Evidence of Ice-Rich Layered Deposits in the Medusae Fossae Formation of Mars

Thomas R. Watters[1*], Bruce A. Campbell[1], Carl J. Leuschen[2], Gareth A. Morgan[3], Andrea Cicchetti[4], Roberto Orosei[5], and Jeffrey J. Plaut[6]

[1]Center for Earth and Planetary Studies, National Air and Space Museum, Smithsonian Institution, Washington, D.C. 20560, USA

[2]CReSIS, The University of Kansas, Lawrence, Kansas 66045, USA

[3]Planetary Science Institute, Tucson, AZ, USA

[4]IAPS, Istituto Nazionale di Astrofisica, 00133, Roma, Italy

[5]IRA, Istituto Nazionale di Astrofisica, 40129, Bologna, Italy

[6]JPL, California Institute of Technology, Pasadena, CA 91109, USA.

*Corresponding author. Thomas Watters watterst@si.edu

Key Points

- MARSIS radar sounder data reveals layering in the Medusae Fossae Formation deposits.
- Layers are likely due to transitions between mixtures of ice-rich and ice-poor dust, analogous to those in Polar Layered Deposits.
- An ice-rich portion of the MFF deposit may contain the largest volume of water in the equatorial region of Mars.

Accepted for Publication in ***Geophysical Research Letters***

Abstract

Subsurface reflectors in radar sounder data from the MARSIS instrument aboard the Mars Express spacecraft indicate significant dielectric contrasts between layers in the Martian Medusae Fossae Formation (MFF). Large density changes that create dielectric contrasts are less likely in deposits of volcanic ash, eolian sediments, and dust, and compaction models show that homogeneous fine-grained material cannot readily account for the inferred density and dielectric constant where the deposits are more than a kilometer thick. The presence of subsurface reflectors is consistent with a multi-layer structure of an ice-poor cap above an ice-rich unit analogous to the Martian Polar Layered Deposits. The volume of an ice-rich component across the entire MFF below a 300-600 m dry cover corresponds to a global equivalent layer of water of ~1.5 to ~2.7 m or ~30% to 50% of the total estimated in the North Polar cap.

Plain Langue Summary

The Medusae Fossae Formation, located near the equator of Mars along the dichotomy boundary between the lowlands of the northern hemisphere and the cratered highlands of the southern hemisphere, is one of the largest and least understood deposits on Mars. The MARSIS radar sounder detects echoes in Medusae Fossae Formation deposits that occur between the surface and the base which are interpreted as layers within the deposit like those found in Polar Layered Deposits of the North and South Poles. The subsurface reflectors suggest transitions between mixtures of ice-rich and ice-poor dust analogous to the multi-layered, ice-rich polar deposits. An ice-rich part of the Medusae Fossae Formation deposit corresponds to the largest volume of water outside the polar caps, or a global equivalent layer of water of ~1.5 to ~2.7 m.

1 Introduction

The Mars Advanced Radar for Subsurface and Ionospheric Sounding instrument (MARSIS) onboard the European Space Agency's (ESA) Mars Express spacecraft (Picardi et al, 2005) has successfully probed the ice-rich North and South Polar Layered Deposits (NPLD and SPLD) (Picardi et al, 2005; Plaut et al., 2007), the Dorsa Argentea Formation (Whitten et al., 2020) the Hematite-Bearing Plains and Etched Plains deposits of Meridiani Planum (Watters et al., 2017), and the Medusae Fossae Formation (MFF) (Watters et al., 2007) (Text S1 in Supporting Information). The MFF is the most mysterious, and its origin the most controversial, of these deposits. The MFF deposits are broadly distributed along the dichotomy boundary (Fig. 1) and are thought to be either volcanic ashfall deposits (Bradley et al., 2002; Hynek et al, 2003; Kerber et al., 2011; Ojha & Lewis, 2018; Ojha & Mittelholz, 2023), eolian sediments (Tanaka, 2000), dust deposits (Ojha et al., 2018), or an ice-rich deposit analogous to the PLD (Schultz & Lutz, 1988; Head & Kreslavsky, 2004). It has also been suggested that MFF consists of massive deposits of pumice that floated in a northern ocean and accumulated along the dichotomy boundary (Mouginis-Mark & Zimbelman, 2020). Dielectric properties derived from MARSIS and SHARAD radar sounder data do not rule out ice-rich MFF deposits (Watters et al., 2007; Carter et al., 2009: Orosei, et al., 2015; Campbell & Morgan, 2018), with a possible 300-600 m thick insulating cover of dry sediment (Campbell et al. 2021).

Central to the question of massive ice within the MFF is whether such a two-layer model is supported by internal density changes that create significant dielectric contrasts, and whether the overall dielectric behavior with thickness can be explained by a self-compacting, ice-poor sedimentary unit of uniform grain size. Early MARSIS work showed reflecting interfaces in just two locales (Watters et al., 2007). An absence of internal dielectric contrasts would be expected for

88 an ice-poor volcanic ash, eolian sediment, or dust unit because the depositional mechanisms involved
89 are less likely to result in significant density/dielectric layering contiguous over horizontal distances
90 comparable to the MARSIS footprints (i.e., 10s of km). For the case of an ice-poor sedimentary
91 unit, the bulk density is dependent on the particle density, the porosity of the deposit, and the
92 degree of compaction.

93 We present two-dimensional subsurface profiles from MARSIS sounding data that show
94 strong radar reflections correlated with abrupt density/dielectric changes over lateral distances up
95 to 100s of km in units of the MFF. Clutter simulations confirm that these echoes likely do not
96 come from off-nadir reflections by surface topography. We also derive a new estimate of the
97 maximum thickness of the MFF deposits and compare their bulk real dielectric constant (inferred
98 from the value required to yield a projected basal boundary consistent with the regional slope) to
99 the results of compaction models for ice-free deposits with a range of grain size and initial
100 porosity.

101 ## 2 Results

102 MARSIS SS3-mode data acquired over the last decade and targeted Super-Frame Mode
103 SFM data (see Text S2, Fig. S1) acquired over the last three years provide new insight into the
104 nature of the MFF deposits. The three largest contiguous MFF deposits are Lucus Plunum
105 (~5°S, 185°E), Medusae Fossae-Eumenides Dorsum (~0°N, 200°E), and Amazonis Mensa-
106 Gordii Dorsum (~0°N, 215°E) where deposits extend to Gigas Fossae (Fig. 1). A survey of
107 MARSIS data shows evidence of layering in all three units (Fig. 1, 2). In each case, the depth
108 below the surface is estimated from the time delay Δt using the speed of light corrected by the
109 mean dielectric constant (see Text S3).

Of the large MFF deposits, the subsurface of Amazonis Mensa is the most striking with multiple echoes interpreted to be evidence of layering (Fig. 2A, B). At least two, and possibly more, undulating echoes suggest a complex sequence or group of layers in Amazonis Mensa. Multiple internal echoes in similar patterns have been found in both the SPLD (Fig. 2C) and NPLD (Fig. 2D) (Picardi et al, 2005; Plaut et al., 2007). The most prominent echoes are at Δt ~4.3 μs (AM1) and ~9.9 μs (AM2) in SS3 orbit 10216, interpreted as two dielectric interfaces above a basal contact at ~17.0 μs (AM3) (Fig. 2A, Fig. S2). The reflector at Δt ~17.0 μs (AM3) is continuous with an ~4.3 μs (AG-V1) echo beneath deposits in the extensive lower-elevation area separating Amazonis Mensa and Gordii Dorsum (Fig. 2A, 2B, Fig. S2). A reflector identified in SHARAD orbit 24211_1 (Lalich et al., 2022) that crosses the valley, further to the north where the MFF deposits thin, correlates with the basal contact found in 10216 and adjacent orbit 13416 (Fig. S3A, B). The deeper reflector (A-GV2) in the region, also noted in MARSIS track 4117 (Watters et al., 2007), is below that SHARAD-detected base (Fig. S4D) and may be linked with earlier deposits of MFF material (Morgan et al., 2015). Evidence of multiple layers in Amazonis Mensa is found in the northwest (Fig. S5) and northeastern flanks of the deposits (SFM orbit 19681, Fig. 2E). Here, two subsurface echoes, at Δt ~4.3 μs and at ~8.5 μs, occur above a basal echo at ~14.2 μs (Fig. S6).

Although MARSIS and SHARAD both detect the Δt ~4.3 μs (AG-V1) reflector in the low-elevation area and trace it under Amazonis Mensa massif, SHARAD (Fig. 2A) does not detect dielectric interfaces at smaller delays to match those in the MARSIS data. This intriguing result may be connected with the very different wavelengths (~60-100 m for MARSIS and ~20 m for SHARAD) and delay resolutions (1-μs for MARSIS versus 0.1 μs for SHARAD) of the two instruments, potentially leading to different patterns of multi-layer echo enhancement within

a delay cell (Campbell & Morgan, 2018; Lalich et al., 2022). In simple terms, we propose that the MARSIS-observed reflections are likely due to a favorable vertical spacing of density changes that reinforce the radar echoes at longer wavelengths over the larger delay cells.

Evidence of layering is also found in the easternmost MFF deposits near Gigas Fossae (Fig. 1, Fig. S7), and in Lucus Planum. Two distinct subsurface echoes at Δt ~8.5 μs and ~12.8 μs are detected in SS3 orbit 18703 (Fig. 1, 2F) (Fig. S8). These are interpreted, respectively, to be echoes from a dielectric contrast at intermediate depth and what we term the "basal" interface, which may lie between the MFF and local plains deposits or simply the deepest penetration of a layered MFF sequence.

In the thinner, westernmost MFF deposits of Zephyria Planum (~0°N, 153°E) (Fig. 1), evidence of an internal reflector is less definitive. A subsurface echo in SFM orbit 19738 at Δt ~5.7 μs may be from a dielectric contrast or a strong sidelobe of the surface echo (Fig. S9). However, an internal reflector is present in the Zephyria Planum deposits in SHARAD orbit 22011 (Campbell et al., 2021).

Evidence of internal layering is not present in all radargrams traversing MFF deposits, due either to the absence of a significant dielectric contrast along track, or lower MARSIS signal gain resulting from spacecraft altitude or ionospheric loss.

2.1 Maximum Thickness and Loss Tangent

Subsurface echoes are also detected in the thick MFF deposits of Eumenides Dorsum (Fig. 1). A subsurface echo in SS3 orbit 18664 at Δt ~5.7 μs is interpreted to be a shallow-depth interface above a deeper (Δt ~20.6 μs) basal echo (Fig. 2G, Fig. S10). Deeper subsurface echoes in Eumenides Dorsum are found in MARSIS SS3 orbits 13240 and 15423 (Fig. 3A, B). Echoes at Δt ~30 μs occur above deeper, apparent basal echoes in these orbits. The basal echoes from

MFF dielectric interfaces identified here are at greater time delay than earlier studies which estimated a maximum penetration depth of 2.5 km over Eumenides Dorsum (Watters et al., 2007). Orbits 13240 and 15423 cross the highest elevations of Eumenides Dorsum and show a sharp transition to a diffuse echo pattern that likely demarks the contact between the MFF deposits and the lowlands volcanic plains (Watters et al., 2007; Tanaka, 2000) (Fig. 3C, D).

The measured Δt between the surface returns and the basal echoes range from ~39.0 μs to 41.8 μs (Fig. S11, S12) with a mean of 40.4 μs and a standard deviation of 1.1 μs (n=8). The maximum relief of MFF deposits above the lowlands volcanic plains is estimated using Mars Orbiter Laser Altimeter (MOLA) topography. The relief is measured between the maximum elevation of the MFF deposits and the lowlands volcanic plains along MOLA profiles, with a mean value along the ground track of orbits 13240 and 15423 of ~3,700±90 m (Fig. S13). This is consistent with MOLA-based estimates of the maximum thickness of MFF deposits of Eumenides Dorsum by Hynek et al. (2003) of at least 3.5 km. The only other deposit the MARSIS radar sounder has penetrated to a depth of 3.7 km is the SPLD (Plaut et al. 2007). The elevation-time delay relationship based on the measurements of maximum relief corresponds to a mean ε' of ~2.7±0.2 (n = 4) (see Text S3), in agreement with previous estimates of 2.9±0.4 based on measurements using MARSIS data over thicknesses up to ~2,500 m (Watters et al., 2007) and ε' of 2 to 3 using SHARAD data (Carter et al., 2009; Campbell et al., 2021). From the echo power at 3,700 m (using band 3) and previous MARSIS measurements (Watters et al., 2007), the attenuation of the MFF is ~0.004 dB/m with a range (from the standard deviation of the slope) of ~0.002 to 0.005 dB/m. This range in attenuation corresponds to a range in loss tangent of ~0.002 to 0.004. A loss tangent of 0.003 is consistent with previous estimates using MARSIS data (Watters et al., 2007) and those obtained using SHARAD data (Campbell and

179 Morgan, 2018; Campbell et al., 2021). Estimates of the loss tangent of the SPLD range from
180 ~0.001 to 0.005 (Plaut et al., 2007).

181 We interpret the dielectric interface seen by both sounders at 4.3 μs in the region between
182 Amazonis Mensa and Gordii Dorsum, and extending to greater time delay under Amazonis
183 Mensa, as the contact between the main MFF deposits and earlier plains-forming flows. The
184 MARSIS reflections at Δt ~4.3 and 5.7 μs (~370 m and ~490 m depth) within Amazonis Mensa
185 are attributed to multiple, roughly horizontal density changes within a 1-μs delay cell that
186 coherently interfere to produce a strong echo at 60-100 m wavelength. We propose that this zone
187 of density changes marks the transition between a 300-600 m thick dry upper cap proposed from
188 SHARAD data and an ice-rich lower unit analogous to the NPLD and SPLD. Reflectors at
189 similar depth in Lucus Planum (Fig. S8), Zephyria Planum (Fig S9), and Medusae Fossae-
190 Eumenides Dorsum (Fig. S10) may indicate a similar change in ice content.

191 ***2.2 Compaction Behavior***

192 The primary alternative hypothesis remains an ice-poor material of some grain size that
193 has low porosity at the upper surface. At grain sizes typical of sand, volcanic ash, or silicate dust
194 particles, a deposit will significantly compact over thicknesses of several kilometers. This self-
195 compaction results in a decrease in porosity and an increase in bulk density, causing a change in
196 the depth-integrated electrical properties (i.e., the average real dielectric constant) of the material
197 (Watters et al., 2017; Campbell et al., 2021; Ulaby, 1988; Morgan et al., 2015). The compaction
198 behavior of example materials is evaluated to 3,700 m, the maximum thickness described above
199 (Fig. 4) (see Text S4).

200 Typical physical properties of these materials (i.e., compressibility k, initial porosity ϕ_o,
201 particle density ρ_p) are given in Table S2. Dust-sized particles experience the most reduction in

porosity and increase in density with depth (Fig. 4A, B). Variations in the assumed initial porosity of ±5%, do not significantly change the compaction profiles, particularly at depths corresponding to the maximum MFF thickness (Fig. 4A, B).

The real dielectric constant ε′ of a fine-grained material as a function of depth can be estimated given a porosity and density profile, because in a compacting deposit the two-way travel time is related to the integral of the effective speed of light over the unit depth (see Text S5). Model results indicate that a 3,700 m thick sequence of sand-sized particles has an apparent $\varepsilon'_a > 4$ while dust or volcanic ash have an $\varepsilon'_a > 5$ (Fig. 4C). This confirms that an ice-poor deposit of uniform grain size cannot readily account for the inferred ε′ of the MFF deposits of 2.9±0.4, and that a large fraction of the thickness beyond a few hundred meters must comprise a minimally compressible material with real dielectric constant of ~3 (Watters et al., 2007; Campbell et al., 2021).

4 Discussion

Our conclusion, reinforcing the SHARAD evidence for a two-layer model with significant ice-rich material at depth would require deposition of a PLD-like deposit at the Martian equator during periods of high obliquity (Schultz & Lutz, 1988; Head & Kreslavsky, 2004; Forget F. et al., 2006). This is supported by several lines of evidence: rhythmic layering in MFF deposits in HiRISE image surveys (Khan & Lewis, 2023); modeling of the Martian paleoclimate indicating that at high obliquity the distribution of stable ground ice and regions of ground-ice stability extends to equatorial latitudes (Aharonson et al., 2022); and epithermal neutron data from the Mars Odyssey Neutron Spectrometer (Wilson et al., 2017), suggesting >40% water equivalent hydrogen (WEH) in some locales (Feldman et al., 2011). Recent neutron data collected by the FREND instrument onboard ESA's Trace Gas Orbiter also suggest high

WEH in some locations near the MFF deposits (Malakhov et al., 2020). The apparent abundance of WEH in the upper tens of centimeters in the MFF near-surface where it is expected to be dry may be due to local enhanced diffusion of water vapor from the deep, ice-rich portion of the deposit. A layer of dust or pyroclastic ash (Campbell et al., 2021; Wilson et al., 2017) could provide the insulating material that preserves the water ice in MFF deposits.

If the lower unit of the MFF is a mix of basaltic dust and water ice, at an upper range of ε' of 3.3 estimated for the deposits (Watters et al., 2007), the volume fraction of dust is likely <20% (see Text S6, Fig. S14), a potentially greater fraction than in the PLD (Plaut et al., 2007). The volume of water in the ice-rich layer derived by subtracting 300 to 600 m of cover from the total volume of the MFF deposits is ~220,000 to 400,000 km^3, or ~30% to 50% of the total estimated water in the NPLD (Brothers et al., 2015). This corresponds to a global equivalent layer of ~1.5 to ~2.7 m (Fig. 5, Table S3). Thus, an ice-rich portion of the MFF deposit may contain the largest volume of water in the equatorial region of Mars.

Acknowledgments

We wish to thank the editor and two anonymous reviewers for their comments and suggestions that greatly improved the manuscript. MARSIS is managed by the Agenzia Spaziale Italiana (ASI) and the National Aeronautics and Space Administration (NASA). The Mars Express mission is managed and operated by the European Space Agency. This work was supported by the Italian Space Agency (ASI) through contract 2019-21-HH.0.

Open Research

Data Availability Statement

Datasets for this research are available in these in-text data citation references: MARSIS (2023) and SHARAD (2021). Processed radargrams and other data are available on the Smithsonian's Figshare site (Watters, 2023).

Supporting Information

Data needed to evaluate the paper are present in the paper and/or the Supporting Information. Data is available on the Smithsonian's Figshare site (Watters, 2023).

References

Aharonson O. et al., (2022) Milankovitch Forcing of Equilibrium Ground-Ice on Mars, *LPSC 53*, Abstract #2002.

Bradley, B.A., Sakimoto, S.E.H., Frey, H., Zimbelman, J.R., (2002) Medusae Fossae Formation: New perspectives from Mars Global Surveyor. *J. Geophys. Res*., **107**, 5058.

Brothers, T.C. Holt, J.W. Spiga, A. (2015) Planum Boreum basal unit topography, Mars: Irregularities and insights from SHARAD, *J. Geophys. Res.* **120,** 1357–1375, doi:10.1002/2015JE004830.

Campbell, B.A. & Morgan, G.A. (2018) Fine-scale layering of Mars polar deposits and signatures of ice content in non-polar materia from multi-band SHARAD data processing, *Geophys. Res. Lett.* **45**, 1759–1766.

Campbell, B.A., Watters, T.R., Morgan, G.A. (2021) Dielectric Properties of the Medusae Fossae Formation and Implications for Ice Content, *J. Geophys. Res*., doi:10.1029/2020JE006601.

Carter L.M. *et al*., (2009) Shallow Radar (SHARAD) sounding observations of the Medusae Fossae Formation, Mars, *Icarus* **199**, 295-302.

Feldman W.C. et al., (2011) Mars Odyssey neutron data: 2. Search for buried excess water ice deposits at nonpolar latitudes on Mars, *J. Geophys. Res.* **116**, E11009.

Forget F. *et al*., (2006) Formation of Glaciers on Mars by Atmospheric Precipitation at High Obliquity, *Science* **311**, 368-37.

Head J.W. & Kreslavsky M., (2004) Medusae Fossae Formation: Ice-Rich Airborne Dust Deposited During Periods of High Obliquity, *Lunar Planet. Sci.* **35**, 1635 (abstr.).

Hynek, B.M., Phillips, R.J., Arvidson, R.E. (2003) Explosive volcanism in the Tharsis region: Global evidence in the martian geologic record, *J. Geophys. Res.* **108**, 5111.

Kerber L., et al., (2011) The dispersal of pyroclasts from Apollinaris Patera, Mars: Implications for the origin of the Medusae Fossae Formation, *Icarus* **216**, 212–220.

Khan, S.Y. and Lewis, K.W. (2023) Distribution of Layered Outcrops in the Medusae Fossae Formation, Mars, LPSC 54, Abstract #3027.

Lalich, D.E., Hayes, A.G. & Poggiali, V. (2022) Explaining Bright Radar Reflections Below The South Pole of Mars Without Liquid Water. *Nat Astron* **6**, 1142–1146.

Malakhov A.V. et al., (2020) Ice Permafrost "Oases" Close to Martian Equator: Planet Neutron Mapping Based on Data of FREND Instrument Onboard TGO Orbiter of Russian-European ExoMars Mission, *Astronomy Lett.*, **46**, 407–421 https://doi.org/10.1134/S1063773720060079.

MARSIS (2023) The European Space Agency Mars Express: MARSIS. NASA Planetary Data System. https://pdsgeosciences.wustl.edu/missions/mars_express/marsis.htm [Dataset]

Mouginis-Mark, P.J. & Zimbelman, J.R. (2020) Rafted pumice: A new model for the formation of the Medusae Fossae Formation, Mars, *Icarus* **343**, 113684.

Morgan, G.A. *et al*., (2015) Evidence for the episodic erosion of the Medusae Fossae Formation within the youngest volcanic province on Mars, *Geophys. Res. Lett*. **42**, 7336–7342.

Ojha, L. & Lewis, K. (2018) The density of the Medusae Fossae Formation: Implications for its composition, origin, and importance in martian history, *J. Geophys. Res.* **123**, 1368–1379.

Ojha, L. & Mittelholz, A. (2023) Insight into the formation mechanism of the Medusae fossae formation on Mars from magnetic field data, Icarus, **395**, https://doi.org/10.1016/j.icarus.2023.115471.

Ojha L. et al., (2018) The Medusae Fossae Formation as the single largest source of dust on Mars, *Nature Comm.* **9**, 2867, doi:10.1038/s41467-018-05291-5.

Orosei, R. et al., (2015) Mars advanced radar for subsurface and Ionospheric sounding (MARSIS) after nine years of operation: A summary, *Planet. Space Sci.* **112**, 98–114.

Picardi G. *et al* Picardi G. *et al*., (2005) Radar soundings of the subsurface of Mars, *Science* **310**, 1925.

Plaut J.J. *et al*., (2007) Subsurface radar sounding of the south polar layered deposits of Mars, *Science* **316**, 92.

Tanaka, K.L. (2000) Dust and Ice Deposition in the Martian Geologic Record, *Icarus* **144**, 254–266.

Tanaka K.L. *et al*., (2014) Geologic map of Mars: U.S. Geological Survey Geologic Investigations 3292, https://dx.doi.org/10.3133/sim3292.

Terzaghi K. & Peck, R.B. *Soil Mechanics in Engineering Practice*, John Wiley & Sons, New York (1967).

Schultz P.H. & Lutz, A.B. (1988) Polar wandering of Mars, *Icarus* **73**, 91.

SHARAD (2023) Mars Reconnaissance Orbiter: SHARAD. NASA Planetary Data System. https://pds-geosciences.wustl.edu/missions/mro/sharad.htm [Dataset]

Ulaby F.T. *et al*., *Microwave Dielectric Spectrum of Rocks* (Univ. of Michigan, Ann Arbor, 1988).

Wilson J.T. et al., (2017) Equatorial locations of water on Mars: Improved resolution maps based on Mars Odyssey Neutron Spectrometer data, *Icarus* **299**, 148–160.

Watters, T.R. (2023). Evidence of Ice-Rich Layered Deposits in the Medusae Fossae Formation of Mars. National Air and Space Museum. Figure. https://doi.org/10.25573/data.21699452.v1 [Dataset]

Watters T.R. *et al*., (2007) MARSIS radar sounding of the Medusae Fossae Formation: A unique deposit on Mars, *Science* **318**, 1125–1128.

Watters T.R. *et al.*, (2017) Radar sounder evidence for a thick, porous sediments in Meridiani Planum and Implications for ice-filled deposits on Mars, *Geophys. Res. Lett.* **44**, 9208–9215.

Watters T.R. et al., (2019) MARSIS Subsurface Radar Sounding of Medusae Fossae Formation Deposits on Mars: Ice Rich or Ice Poor, That is the Question**,** LPSC 48, Abstract #2666.

Whitten, J.L. Campbell, B.A. Plaut, J.J. (2020) The Ice Content of the Dorsa Argentea Formation from Radar Sounder Datau, Geophys. Res. Lett. 47.

References from the Supporting Information

366 Andrews-Hanna, J.C. et al., Meridiani Planum and the global hydrology of Mars, *Nature* **446**,
367 163–166 (2007).
368
369 Athy, L.F., (1930) Density, porosity and compaction of sedimentary rocks, *Amer. Assoc. Petro.*
370 *Geophys. Bull.* **14**, 1-24.
371
372 Binder A.B. & Lange, M.A. (1980) On the Thermal History, Thermal State, and Related
373 Tectonism of a Moon of Fission Origin, *Moon* **17**, 29-45.
374
375 Brouet Y. *et al*., (2019) A laboratory-based dielectric model for the radar sounding of the martian
376 subsurface, Icarus **321**, 960-973.
377
378 Campbell, B.A., Watters, T.R., Morgan, G.A. Dielectric Properties of the Medusae Fossae
379 Formation and Implications for Ice Content, *J. Geophys. Res*.,
380 doi:10.1029/2020JE006601 (2021).
381
382 Carter L.M. *et al*., (2009) Shallow Radar (SHARAD) sounding observations of the Medusae
383 Fossae Formation, Mars, *Icarus* **199**, 295-302.
384
385 Clifford, S.M. (1993) A Model for the Hydrologic and Climatic Behavior of Water on Mars, *J.*
386 *Geophys. Res.* **98***,* 10,973-11,016.
387
388 Domenico P.A. & Mifflin, M.D. Water form low-permeability sediments and land subsidence,
389 *Water Resources Res.* **1**, 563-576 (1965).
390
391 Freeze R.A. & Cherry, J. *Groundwater,* Pearson Publishing (1979).

392 Grotzinger, J.P. et al., (2015) Deposition, exhumation, and paleoclimate of an ancient lake
393 deposit, Gale crater, Mars, Science 350 DOI: 10.1126/science.aac7575.
394
395 Gromov, V.V., Physical and mechanical properties of Lunar and Planetary Soils, in *Laboratory*
396 *Astrophysics and Space Research*, edited by Ehrenfreund P. et al.) pp. 121-142, Kluwer
397 Academic Publishers (1999).
398
399 Hantschel T. & Kauerauf, A. I. (2009) *Fundamentals of Basin and Petroleum Systems*
400 *Modeling,* Springer-Verlag, Berlin.
401
402 Heggy E. *et al*., (2008) On the Dielectric Properties of Dust and ice-dust mixtures: Experimental
403 Characterzation of the Martian Polar Layered Deposits Analog Materials, *LPSC 38th*,
404 Abstract #1756.
405
406 Hapke B. & Sato, J. The porosity of the upper lunar regolith, *Icarus* **273**, 75-83 (2016).
407
408 Head J.W. & Kreslavsky M., Medusae Fossae Formation: Ice-Rich Airborne Dust Deposited
409 During Periods of High Obliquity, *Lunar Planet. Sci.* **35**, 1635 (abstr.) (2004).
410

411 Jordan, R. et al., (2009) The Mars express MARSIS sounder instrument, *Planet. Space. Sci.* **57**,
412 1975-1986.
413
414 Kawabata E. et al., Identifying multiple eruption phases from a compound tephra blanket: an
415 example of the AD1256 Al-Madinah eruption, Saudi Arabia, *Bull. Volcanology* **77**,
416 doi10.1007/s00445-014-0890-y (2015).
417
418 Lewis K.W. et al., (2019) A surface gravity traverse on Mars indicates low bedrock density at
419 Gale crater, *Science* **363,** 535–537.
420
421 McMichael J.G., Gim, Y. Arumugam D.D. and Plaut, J.J. *2017 IEEE Radar Conference*
422 *(RadarConf)*, 2017, pp. 0873-0878, doi: 10.1109/RADAR.2017.7944326.
423
424 Mitchell, J.K. et al., Mechanical properties of lunar soil: Density, porosity, cohesion, and angle
425 of internal friction, *Proc. Lunar Sci. Conf.* 3, 3235-3253 (1972).
426
427 Morgan, G.A. *et al*., (2015) Evidence for the episodic erosion of the Medusae Fossae Formation
428 within the youngest volcanic province on Mars, *Geophys. Res. Lett*. **42**, 7336–7342.
429
430 Paladio-Melosantos M.L.O. et al., in *Fire and Mud: Eruptions and Lahars of ount Pinatubo,*
431 *Philippines*, edited by Newhall, C. G. and Punongbayan, R. S.) Univ. of Washington
432 Press (1997).
433
434 Palmer S.J. & H.W. Wick, *New Zealand Geotechnical Society Symposium*, 240-250 (2003).
435
436 Pender, M. J. et al., (2006) Geotechnical properties of a pumice sand, Soils and Foundations, **46**,
437 69-81.
438
439 Schultz P.H. & Lutz, A.B. Polar wandering of Mars, *Icarus* **73**, 91 (1988).

440 Stillman D.E. et al., (2010) Low-Frequency Electrical Properties of Ice-Silicate Mixtures, *J.*
441 *Phys. Chem.* **114**, 6065-6073.
442
443 Squyres, S.W. et al., In Situ Evidence for an Ancient Aqueous Environment at Meridiani
444 Planum, Mars, *Science* 306, 1709–1714 (2004).

445 Tanaka K.L. *et al*., (2014) Geologic map of Mars: U.S. Geological Survey Geologic
446 Investigations 3292, https://dx.doi.org/10.3133/sim3292.
447
448 Watters T.R. *et al*., MARSIS radar sounding of the Medusae Fossae Formation: A unique deposit
449 on Mars, *Science* **318**, 1125–1128 (2007).
450
451 Watters T.R. *et al.*, Radar sounder evidence for a thick, porous sediments in Meridiani Planum
452 and Implications for ice-filled deposits on Mars, *Geophys. Res. Lett.* **44**, 9208–9215
453 (2017).
454

Wilson T.M. et al., (2012) Volcanic ash impacts on critical infrastructure, *Phys. Chem. Earth,* **45-46**, 5-23.

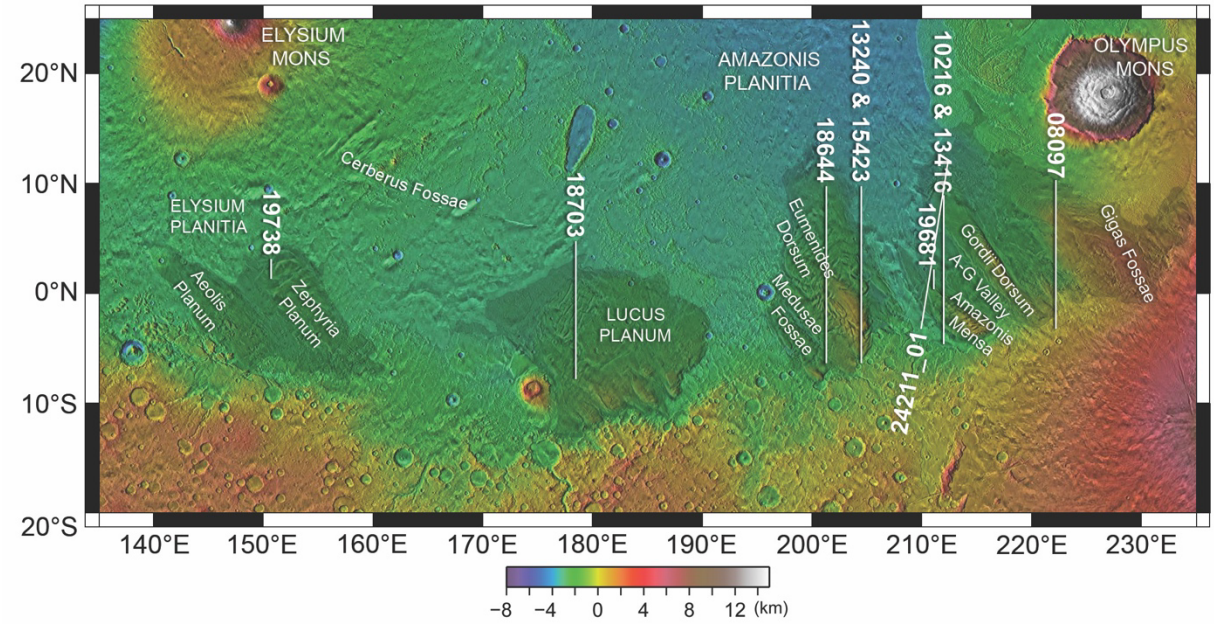

Figure 1. Medusae Fossae Formation deposits along the Martian dichotomy boundary. The locations of MARSIS radargrams are indicated by white lines. Mars Orbiter Laser Altimeter (MOLA) shaded relief map with colorized elevation. The dark shaded areas show the MFF deposit boundaries modified from Tanaka et al. (2014) (multiple unit types were combined).

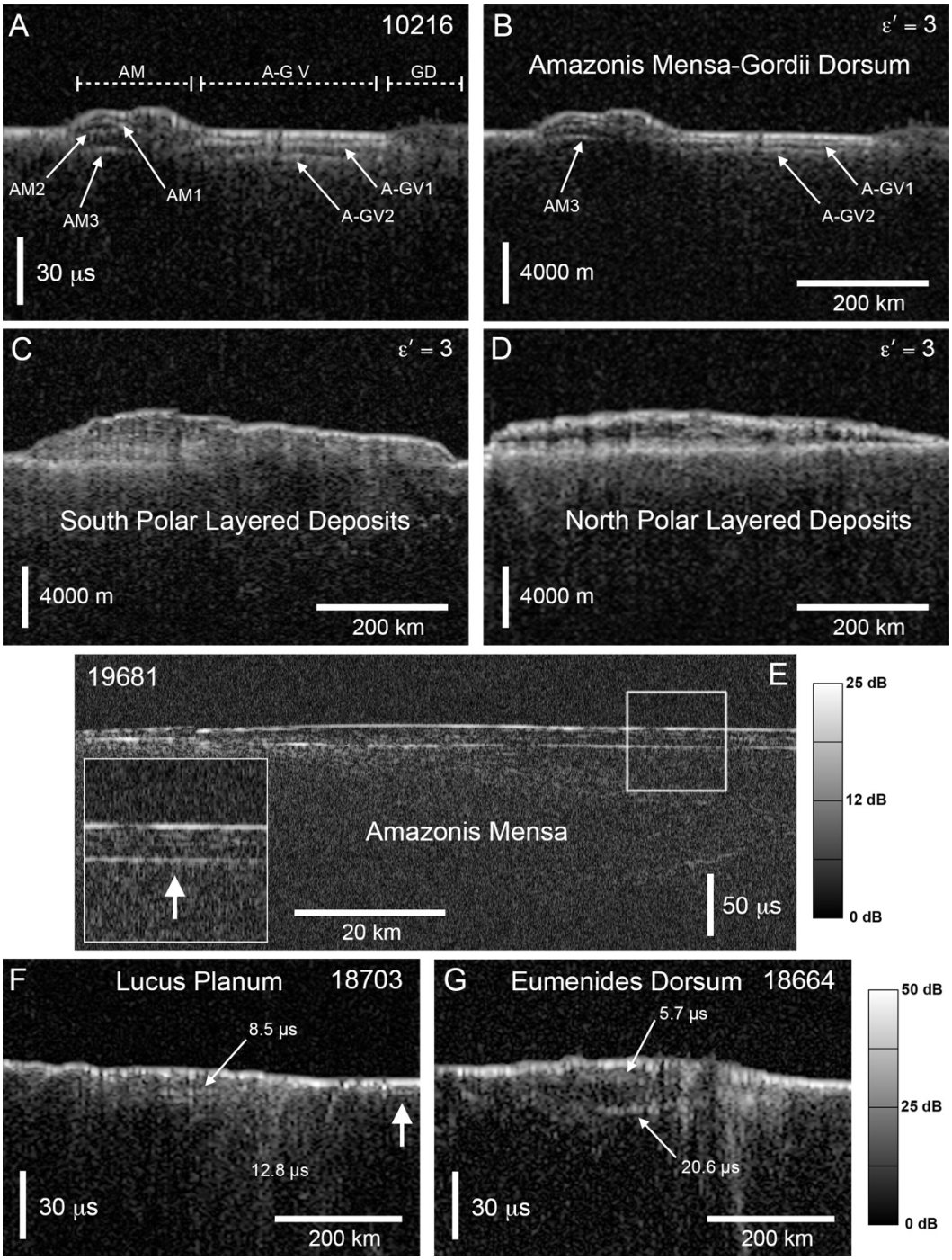

464

465 Figure 2. Radar data collected in SS3-mode and SFM-mode over MFF deposits and the North
466 and South Polar Layered deposits. (A) SS3-mode data from orbit 10216, band 3 over Amazonis
467 Planitia where the vertical axis shows round-trip time delay, Amazonis Mensa is indicated by
468 AM, Gordii Dorsum by GD, and valley between them as A-G V (see Fig. 1). Subsurface echoes

designated AM1 and AM2 are interpreted to be from internal MFF layers (B) the same data from orbit 10216 where the subsurface echoes have been depth corrected to a vertical scale in meters using a real dielectric constant ε′ of 3. Depth corrected radargram shows echo AM3 aligns with echo A-GV1, both interpreted to be from the MFF base. A-GV2 is below the MFF base and may be from earlier deposits of MFF material, (C) data from orbit 06487, band 4 over the South Polar Layered Deposits (SPLD), depth corrected using a ε′ of 3, (D) data from orbit 14019, band 3 over the North Polar Layered Deposits (NPLD), depth corrected using a ε′ of 3, (E) SFM-mode data from orbit 19681, band 2 over a short segment of Amazonis Mensa in round-trip delay time format, (F) data from orbit 18703, band 4 over Lucus Planum in time-delay format, and (G) data from orbit 18664, band 3 over Eumenides Dorsum in time delay format. Subsurface echoes (white arrows) are offset in time-delay from the surface echo and are interpreted to be either nadir reflections from the interface between layers in the MFF deposits or between the MFF base and the lowland volcanic plains material.

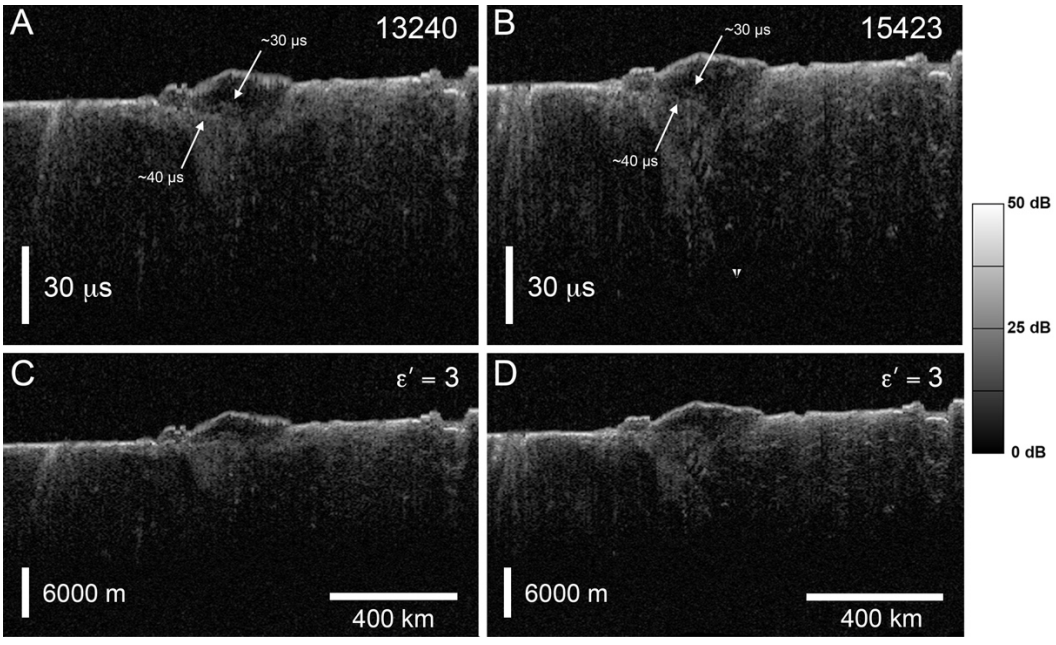

Figure 3. Radar data over Eumenides Dorsum. Radargrams showing MARSIS SS3-mode radargrams from orbits 13240, band 2 (A) and 15423, band 2 (B) with round-trip time delay on the vertical axis. The lower two figures (C and D) show the same MARSIS tracks where the subsurface echoes have been converted to vertical distance using a real dielectric constant of 3. The time delays to the top of the diffuse basal echo (~40 μs) are the largest yet found in sounder data in the MFF deposits. The runout of power with time delay suggests a very rough subsurface interface at the base of the MFF or localized high loss. A subsurface reflector above the basal interface is interpreted to be an internal layer (~30 μs).

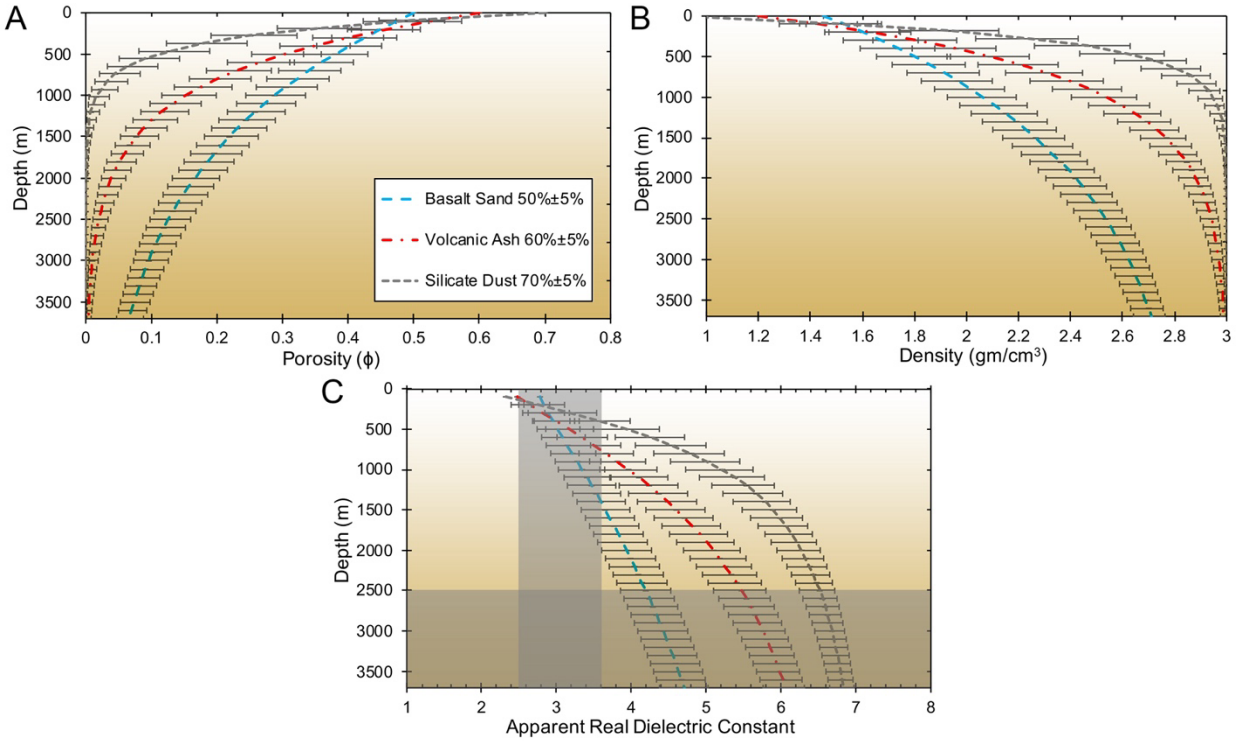

Figure 4. Compaction models for three ideal materials that simulate those commonly proposed for MFF deposits. Porosity (A), density (B), and apparent real dielectric constant (C) curves for three geologic materials: a loose basalt sand (blue large dash), a volcanic ash (red small dash and dot), and a silicate or rock dust (gray small dash). The compaction and density models

incorporate the compressibility of the materials Mars gravity, and the apparent real dielectric constant accounts for the two-way delay time through a material with an increasing index of refraction with depth due to compaction (see Text S4 and Table S2). The error bars show the effect of ±5% variation in the initial porosity. The gray areas in C shows the range in estimates of ε′ for the MFF deposits (2.5 to 3.3) and the range in estimates of the maximum thickness of the deposits (2.5 to 3.7 km). No modeled material has predicted real dielectric constants within the observed range (double shaded area).

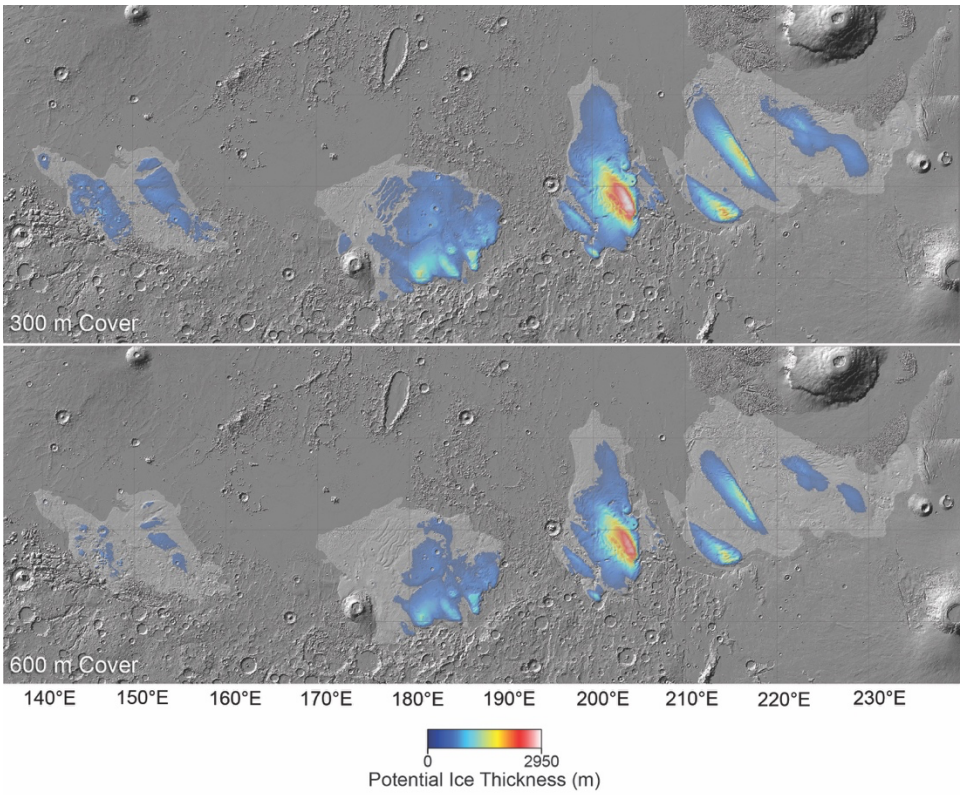

Figure 5. Thickness map of the suspected ice-rich portions of the MFF deposits. MFF deposit boundaries are modified from Tanaka et al. (2014) (multiple unit types were combined and some of the boundaries adjusted). The paleo (pre-MFF) surface was estimated, and 300 m and 600 m of dry cover subtracted to estimate the thickness of the proposed ice-rich layer. The total ice

510 volume of is estimated to be ~2.2×10^5 km^3 (600 m removed) to ~4.0×10^5 km^3 (300 m removed)
511 which corresponds to a GEL of water of ~1.5 to ~2.7 m (see Table S2). The locations of
512 reflectors in orbits 13240 and 15423 (Figs. S10, S11) correspond to the thickest sections of MFF
513 deposits in Eumenides in both the 300 and 600 m cover maps. The greatest volume of the total
514 water in the MFF deposits is in Eumenides Dorsum (Table S2).
515

Geophysical Research Letters

Supporting Information for

Evidence of Ice-Rich Layered Deposits in the Medusae Fossae Formation of Mars

Thomas R. Watters[1*], Bruce A. Campbell[1], Carl J. Leuschen[2], Gareth A. Morgan[3], Andrea Cicchetti[4], Roberto Orosei[5], and Jeffrey J. Plaut[6]

[1]Center for Earth and Planetary Studies, National Air and Space Museum, Smithsonian Institution, Washington, D.C. 20560, USA

[2]CReSIS, The University of Kansas, Lawrence, Kansas 66045, USA

[3]Planetary Science Institute, Tucson, AZ, USA

[4]IAPS, Istituto Nazionale di Astrofisica, 00133, Roma, Italy

[5]IRA, Istituto Nazionale di Astrofisica, 40129, Bologna, Italy

[6]JPL, California Institute of Technology, Pasadena, CA 91109, USA.

Contents of this file

Introduction

The supporting text and figures provide further details on the MARSIS radar sounder instrument, radargrams, and the electrical and physical properties of the Medusae Fossae Formation deposits, and compaction models for loose basaltic sand, volcanic ash, and silicate dust on Mars.

Text S1. Medusae Fossae Formation (MFF) Deposits and Previous Radar Sounder Studies

The MARSIS radar sounder data delineates the surface return and the subsurface interface between the MFF deposits and the underlying terrain, and the suggested transitions between mixtures of ice-rich and ice-poor dust. Nearly all the models for the origin of the MFF deposits involve subaerial deposition. The predicted volatile (i.e., water-ice) content of the deposits at the time of emplacement, however, is very different among such models. The Polar Layered Deposits (PLD) at the south and north poles are known to be ice-rich deposits (Schultz & Lutz, 1988; Head & Kreslavsky, 2004; Watters et al., 2007). Volcanic ash or eolian sand or dust deposits are expected to be initially largely ice-free. If the MFF are purely ash fall deposits, it is difficult to account for their limited distribution in the lowlands along the dichotomy boundary. Localization of ice-rich MFF deposits due to upwelling of vapor-rich air is conceivable (Head & Kreslavsky, 2004), particularly where the change in elevation at the dichotomy boundary is large (Watters et al., 2007). Localization of eolian deposition at the dichotomy boundary is also possible, however, the great thickness of the MFF deposits is more analogous to the PLD (Schultz & Lutz, 1988; Head & Kreslavsky, 2004; Watters et al., 2007). The Hematite-Bearing Plains and Etched Plains of Meridiani are deposits of basaltic sand (Squyres et al., 2004) likely deposited in an aqueous environment (Andrews-Hanna et al., 2007). Compaction models indicate that the dielectric constant of the Meridiani Planum deposits is consistent with a thick layer (1 km) of ice-free, porous, basaltic sand (Watters et al., 2017). However, this is not the case for the MFF deposits (this study).

The MARSIS radar sounder was the first to probe the MFF deposits (Watters et al., 2007). Analysis of the delay time between the MFF surface and subsurface echoes in early MARSIS radargrams showed massive deposits with a thickness of at least 2.5 km were emplaced on generally planar lowlands materials, and that MFF deposits have a real dielectric constant of ~2.9. It was concluded that the real dielectric constant and the estimated dielectric losses were at least not inconsistent with a substantial

component of water ice. However, an anomalously low-density, ice-poor material could not be ruled out. This was because the compaction behavior of thick deposits of the proposed materials had not been evaluated as yet. The SHARAD radar sounder followed with studies of the MFF deposits (Carter et al., 2009). SHARAD radar penetrated up to ~600 m. Analysis of the time delay between surface and subsurface interfaces suggested MFF deposits had a real dielectric constant of ~3.0, consistent with the MARSIS-derived results, and that the upper few hundred meters of the deposits have a high porosity. No evidence of internal layering was found in the SHARAD radargrams, and it was concluded that MFF is not an equatorial analog to Polar Layered Deposits (Carter et al., 2009). Additional studies using SHARAD data employed a split chirp analysis to estimate the loss tangents in different geologic unts suspected to be ice-bearing (Campbell and Morgan, 2018). It was concluded that MFF deposits, lineated valley fill, and lobate debris aprons have low losses consistent with a major component of water ice. In the most comprehensive SHARAD-based study focused on MFF to date, Campbell et al. (2020) concluded that the MFF is a two-layer deposit, with 300–600 m of fine-grained, self-compacting material above a minimally compacting, low-loss material. It was also concluded that the deeper, low-loss material could be ice-rich, or an ice-poor, very coarse-grained sand. The results of these studies are summarized in Table S1. This study was undertaken in an effort to resolve the question of an ice-rich or ice-poor lower unit of the MFF deposits, and to determine if evidence of layering analogous to the Polar Layered Deposits is present in the MFF deposits. This study involved a comprehensive survey of MARSIS radargrams that transect MFF deposits collected since the Watters et al. (2007) study. The survey so combined with compaction modeling for the commonly proposed materials evaluated up to the maximum thickness of the deposits.

Text S2. MARSIS Instrument

The MARSIS instrument is a multi-frequency synthetic aperture orbital sounding radar operating in four frequency bands between 1.8 and 5.0 MHz in its subsurface modes. Its free-space range

resolution is ~150 m, and the cross-track and along track footprint sizes range from 10 to 30 km and 5 to 10 km, respectively (Orosei et al., 2015). The most commonly used of the five subsurface sounding (SS) modes is SS3, consisting of 2 frequency bands and 3 Doppler filters collected on the dipole antenna channel (Orosei et al., 2015; Jordan et al. 2009). Onboard processing in this mode includes pre-summing and conversion of digitized radar echoes to one-byte integers. The instrument also has the capability to collect raw data in 2 frequency bands stored in flash memory (FM). In FM mode, the along-track distance covered is typically ~100 to 250 km, much less than in the SS3 mode. The normal FM radargrams have gaps in coverage, giving the radargrams a picket fence appearance (Watters et al., 2017). The super-frame mode (SFM) provides continuous coverage at the expense of along-track distance, typically <100 km (Figure S1).

Text S3. **Depth Estimates**

The depth to, or thickness of, a layer *h* is related to the measured round-trip delay Δ*t* by

$$h = \Delta t c/(2\sqrt{\varepsilon'}) \quad (1)$$

where *c* is the free-space velocity and ε′ is the real dielectric constant of the material. The time delay is thus given by $\Delta t = 2h\sqrt{\varepsilon'}/c$.

Text S4. **Compaction Model**

Athy's Law describes an exponential decline in porosity as a function of depth in a geologic material (Athy, 1930; Hantschel & Kauerauf, 2009). This relation has been applied to lunar crustal porosity (Binder & Lange, 1980), to the Martian crust and sedimentary rocks (Clifford, 1993; Grotzinger et al., 2015; Lewis et al., 2019), and the compaction of Meridiani Planum deposits (Watters et al., 2017) and the MFF deposits (Ojha & Lewis, 2018; Campbell et al., 2021). Binder and Lange (1980) utilized a porosity decay constant *K* for the Moon, and Clifford (1993) scaled this value to apply to crustal porosity on Mars by the ratio of the acceleration due to gravity for the two bodies. Grotzinger et al. (2015) and Lewis et al. (2019) used *K* values for terrestrial sedimentary rocks and a ratio of the acceleration due to gravity of Earth and Mars. Campbell et al. (2021) employed *K* as the scale parameter to evaluate the

shallow depth compaction of the MFF deposits. Here, we use the adapted version of Athy's Law formulated with effective stress introduced by Watters et al. (2017). The porosity φ as a function of depth is given by

$$\phi = \phi_o \, e^{-k(\rho_b g z)} \quad (2)$$

where φ_o is the initial porosity, k is the compressibility or the inverse of the bulk modulus of the material, ρ_b is the uncompacted bulk density, g is the acceleration due to gravity of Mars, and z is the depth. This equation allows the expected decrease in porosity with depth of specific geologic materials on Mars to be modeled. The relationship between the uncompacted bulk density ρ_b and the initial porosity φ_o is given by $\rho_b = (1 - \varphi_o)\rho_p$ where ρ_p is the density of the particles of the deposit. Thus, ρ_b can be determined if φ_o and ρ_p are known.

Typical physical properties of the three ideal materials modeled are given in Table S2. A well sorted eolian sand is approximated using φ_o = 0.5 (Freeze and Cherry, 1979), and k = 0.1 MPa^{-1} (Domenico & Mifflin, 1965). Using a ρ_p of 2.9 gm/cm^3, the derived ρ_b is 1.45 gm/cm^3, in good agreement with measured ρ_b of 1.43 gm/cm^3 (Terzaghi & Peck, 1967) and is consistent with the bulk porosity of the regolith analyzed by the Viking Landers (Clifford, 1993). The estimated φ_o of volcanic ash is 0.6, in good agreement with reported measured values (φ_o = 0.7) (Kawabata et al., (2015), with a ρ_p of 3.0 gm/cm^3 the derived ρ_b is 1.2 gm/cm^3, in agreement with values for tephra falls (Kawabata et al., 2015; Paladio-Melosantos M.L.O. et al., 1997; Wilson T.M. et al., 2012). A value for the compressibility of volcanic ash of 0.3 MPa^{-1} is used (Palmer & Wick, 2003) (Table S2). Lunar regolith is used to approximate silicate or rock dust with values of φ_o = 0.7 and ρ_p = 3.0 gm/cm^3 with a derived ρ_b is 0.9 gm/cm^3 well approximate the measured value of 1.0 gm/cm^3 (Mitchell, et al., 1972; Hapke & Sato, 2016). A value for the compressibility of 1.0 MPa^{-1} lunar regolith. This value is likely a lower limit with much larger values of k up to 8 MPa^{-1} possible (Gromov, 1999). The compressibility of common sedimentary rocks (i.e., shale, siltstone, and sandstone) ranges from ~0.027 to 0.1 MPa^{-1} (Hantschel & Kauerauf, 2009). Pumice sand was also

examined, but because pumice sand grains have significant intrinsic porosity the compaction behavior is difficult to model. However, it has been shown that at relatively low confining pressures of a few hundred kPa significant crushing of the grains occurs (Pender et al., 2006). Confining pressures of several hundred kPa are reached at shallow depths <100 m on Mars even with the low bulk density of pumice. Crushed grains will significantly change the compressibility and bulk density and thus, the compaction characteristics change to likely those resembling volcanic ash (Fig. 4).

The compaction curves show that well-sorted sand has the least reduction in porosity and silicate dust the most reduction with depth (Fig. 4A). This is also the case for the density. The curve for silicate dust becomes asymptotic at ~1,500 m (Fig. 4B). Volcanic ash at a depth of ~1,000 m is predicted to reach a density of ~2.4 gm/cm^3, and at 3,700 m nearly reaches the particle density of 3.0 gm/cm^3 (Fig. 4B). It should be noted that the compaction models presented here are not intended to include all possible materials or the full range of uncertainty in the model parameters, only plausible examples of those commonly proposed for the MFF deposits.

Text S5. **Apparent real dielectric constant**

The real dielectric constant of geologic materials increases with an increase in ρ_b and is approximated by $\varepsilon' = 1.96^{\rho b}$ (Ulaby et al., 1988). Thus, ε' can be related to a porous material with a particle density ρ_p and porosity φ by

$$\varepsilon' = 1.96^{(1-\phi)\rho_p} \quad (3)$$

In order to evaluate the three commonly cited geologic materials proposed for the MFF deposits, compaction curves for well-sorted sand, volcanic ash, and silicate (lunar-like) dust are modeled.

The change in dielectric constant of a compacting material will have an "apparent" bulk value for any given two-way travel time, based on the assumption of constant ε'. The round-trip travel time in such a compacting medium is:

$$T = \frac{2}{c}\int_0^Z \sqrt{\varepsilon'(z)}\, dz \quad (4)$$

Where *c* is the speed of light in vacuum and *Z* is the maximum depth. If we assume the layer has a uniform dielectric constant at a given depth, then the "apparent" bulk value is given by:

$$\varepsilon'_a = \left(\frac{1}{Z}\int_0^Z \sqrt{\varepsilon'(z)}\, dz\right)^2 \quad (5)$$

A plot of apparent ε'_a as a function of depth for the three modeled materials is shown in Figure 4C. The model results indicate that at 3,700 m, basalt sand has an apparent $\varepsilon'_a > 4$ and volcanic ash and silicate dust an apparent $\varepsilon'_a > 5$. Even at the lower estimate of the maximum thickness of the MFF deposits of 2.5 km, none of the modeled materials can account for the inferred dielectric constant of the deposits (Fig. 4C).

Text S6. **Volume Fraction of Dust**

The real dielectric constant of the MFF deposits can be used to constrain the percent of dust if the deposits are a mix of silicate or basaltic dust and water ice. Using the mixing power law of Stillman et al. (2010)

$$\varepsilon'_n = (\varepsilon'_{dust}{}^{\frac{1}{\gamma}} \times \Phi_{dust} + \varepsilon'_{ice}{}^{\frac{1}{\gamma}} \times \Phi_{ice} + \varepsilon'_{air}{}^{\frac{1}{\gamma}} \times \Phi_{air})^{\gamma} \quad (6)$$

where Φ_{dust}, Φ_{ice}, Φ_{air} are the fractional volumes of each component and γ is the exponent equal to 2.7 determined for ice-sand mixtures. Heggy et al. (2008) estimates the real dielectric constants of basaltic dust at 2 MHz is 4.91 at –20°C and 5.08 at –70°C. Assuming these values for ε'_{dust}, $\varepsilon'_{ice} = 3.0$ and $\varepsilon'_{air} = 1.0$, ε'_n as a function of Φ_{dust} and Φ_{ice}, assuming $\Phi_{air} = 0$, are shown in Fig. S14. Over the range of ε′ determined for the MFF deposits (2.5 to 3.3) that includes the additional ε′ determined for Eumenides Dorsum (2.7), the volume fraction of dust is from 0% to a maximum of <20% (Fig. S14). A volume fraction of dust that does not exceed 20% at the upper end of the range of ε′ for the MFF deposits is generally consistent with estimates of ε′ as a function of porosity for a mix of 24% JSC Mars-1 Martian soil simulant and ice

(see Brouet et al., 2019, Fig. 7). If correct, this suggests that the dust/ice mixture of the lower unit of the MFF deposits may consist of as much as ~75% volume fraction ice.

Table S1. Summary of Past Radar Sounder Studies

Article	Sounder Data	Findings
Watters et al. (2007)	MARSIS	MFF has low permittivity and is composed of large amounts of ice or is an anomalously low-density material.
Carter et al. (2009)	SHARAD	Inferred low permittivity values suggest that the upper few hundred meters of the MFF have a high porosity
Campbell & Morgan (2018)	SHARAD	MFF, lineated valley fill, and lobate debris aprons exhibit low losses consistent with a major component of water ice
Campbell et al. (2021)	SHARAD	MFF is a two-layer deposit, with 300–600 m of fine-grained, self-compacting material above a minimally compacting, low-loss material

Table S2. Typical Physical Properties of Unconsolidated Materials Modeled

Property	Basalt Sand	Volcanic Ash	Silicate Dust
k	0.1 MPa^{-1} (*1*)	0.3 MPa^{-1} (*2*)	1.0 MPa^{-1} (*3*)
φ_o	0.5 (*4*)	0.6 (*5*)	0.7 (*6, 7*)
ρ_p	2.9 gm/cm^3	3.0 gm/cm^3	3.0 gm/cm^3
ρ_{bulk}*	1.45 gm/cm^3	1.2 gm/cm^3	0.9 gm/cm^3

*Note that ρ_{bulk} is derived from the particle density ρ_p and the initial, uncompacted porosity φ_o.

1. Domenico & Mifflin (1965).
2. Palmer & Wick (2003).
3. Gromov (1999).
4. Freeze & Cherry (1979).
5. Kawabata E. et al. (2015)
6. Mitchell et al. (1972).
7. Hapke & Sato (2016).

Table S3. Estimates of the total volume of ice in the MFF deposits

MFF Deposit	Cover Depth (m)	Surface Area Ice (km^2)	Volume Ice (km^3)	GEL* (m)	Cover Depth (m)	Surface Area Ice (km^2)	Volume Ice (km^3)	GEL* (m)
Aeolis/ Zephyria	300	151551	32765	0.23	600	39717	4900	0.03
Lucus Planum	300	219222	92227	0.64	600	125379	42279	0.29
Medusae/ Eumenides	300	275427	208256	1.44	600	201159	136414	0.95
Amazonis/ Gordii	300	115641	62846	0.44	600	72747	35066	0.24
Totals		761841	396094	2.74		439002	218659	1.52

*GEL is the estimate of the Global Equivalent Layer of liquid water on the surface of Mars.

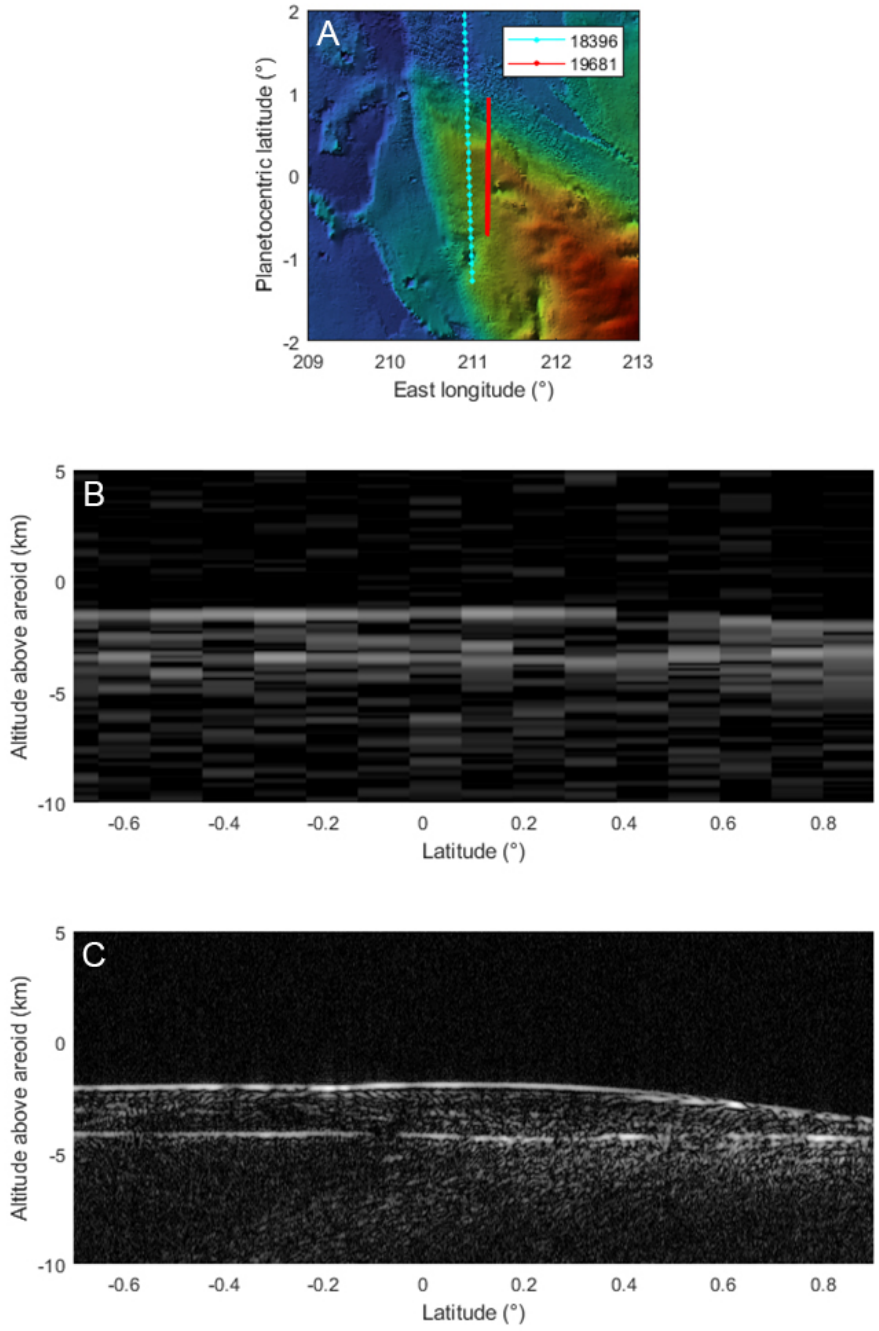

Figure S1. Comparison between on-board processed and raw MARSIS echoes. (a) Shaded relief map of a portion of Amazonis Mensa, showing the ground tracks of orbits 18396 and

19681. (b) Detail of radargram of orbit 18396, in which only on-board processed data have been downlinked. (c) Detail of radargram of orbit 19681, in which raw data were acquired using the super-frame mode and sent to ground. (b) and (c) have been drawn with the same horizontal and vertical scale and extend for the same range of latitudes.

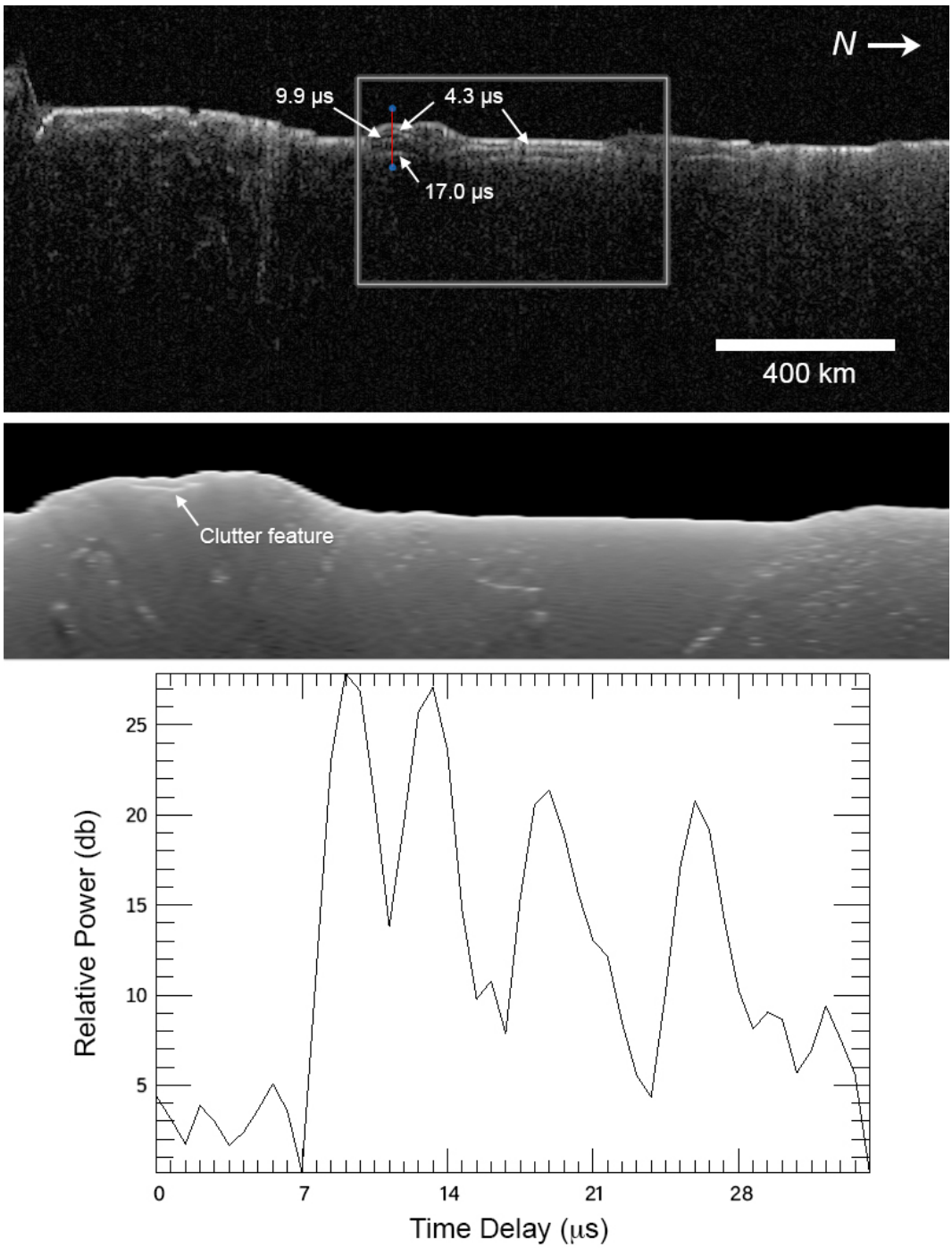

Figure S2. Radargram, clutter simulation, and plot of the relative echo power versus time delay for MARSIS SS3 orbit 10216, band 3. The orbit crosses deposits of Amazonis Mensa-Gordii Dorsum (see Fig. 1, 2A). The four peaks in relative power are interpreted to be the surface return (largest peak) and three subsurface echoes, the two echoes closest in time dela to the peak echo are interpreted to be layers in

the deposits and the echo at greatest time delay is the basal interface. Three distinct subsurface echoes at a Δt of ~4.3 μs, ~9.9 μs, and ~17.0 μs correspond to depths of ~370 m, ~860 m, and ~1470 m, respectively assuming a real dielectric constant ε′ of ~3. A clutter simulation (McMichael et al., 2017) generated using MOLA topography is shown in the middle panel (the approximate area of the model corresponding to the portion of the radargram shown by the rectangular box. The clutter model shows a clutter feature (arrow) located in the Amazonis Mensa massif, but it does not directly correspond to one of the subsurface echoes and cannot be unambiguously attributed to an off-nadir surface feature. (One shallow, off-nadir echo in the clutter model may account for part of a near surface echo in the radargram covering Amazonis Mensa.)

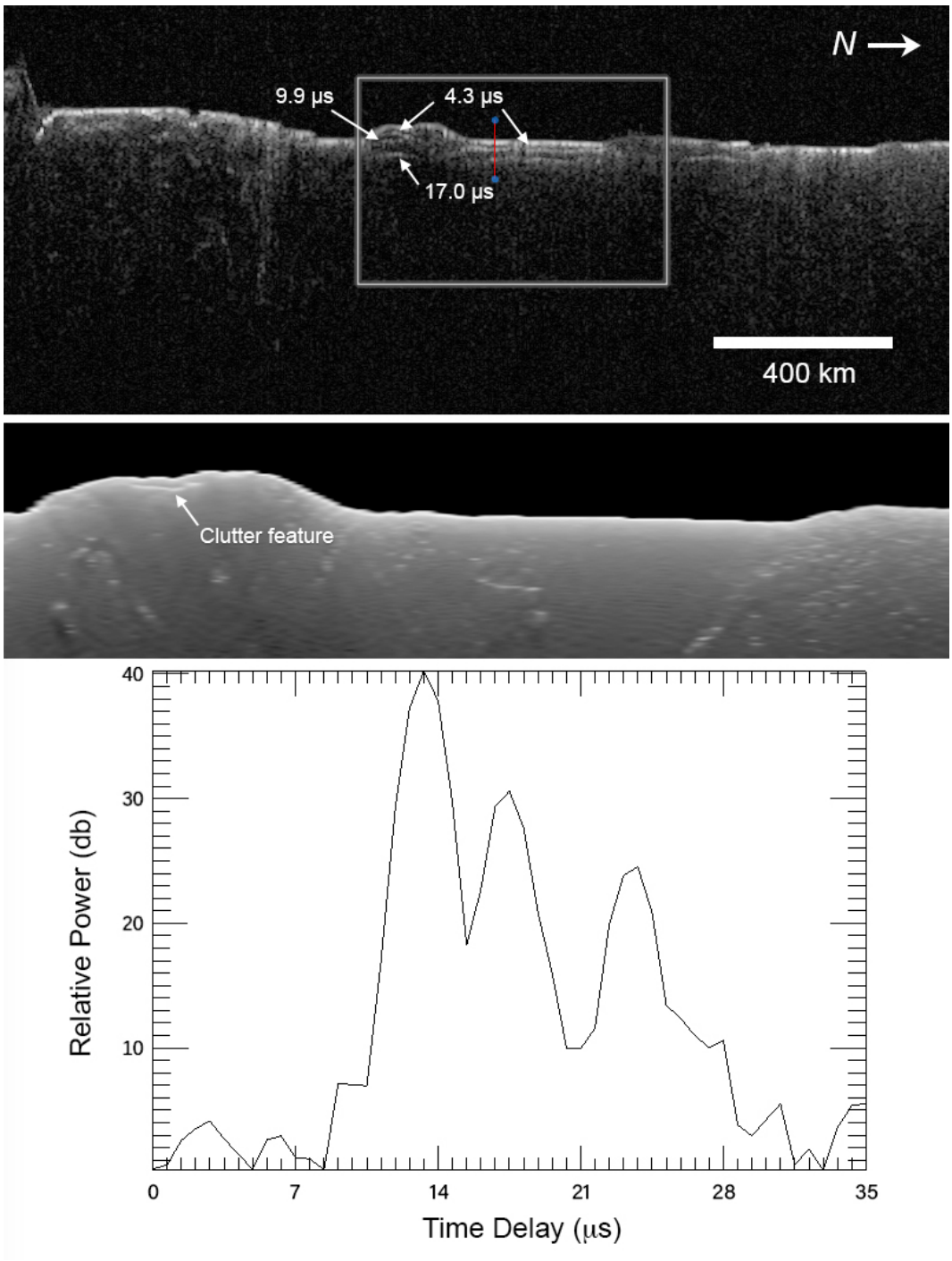

Figure S3. Radargram, clutter simulation, and plot of the relative echo power versus time delay for MARSIS SS3 orbit 10216, band 3. The orbit crosses deposits of Amazonis Mensa-Gordii Dorsum (see Fig. 1, 2A). The three peaks in relative power are interpreted to be the surface return (largest peak) and two subsurface echoes, the echo closest in time delay to the peak echo is interpreted to be a layer that

extends into the valley separating Amazonis Mensa and Gordii Dorsum with the echo at greatest time delay from the surface return is interpreted to be the basal interface. With a Δt of ~4.3 μs and assuming a real dielectric constant ε′ of ~3, the corresponding depth of the valley layer is ~370 m. A clutter simulation (McMichael et al., 2017) generated using MOLA topography is shown in the middle panel (the approximate area of the model corresponding to the radargram is show by the rectangular box). The clutter model shows a clutter feature (arrow) located in the Amazonis Mensa massif, but it does not directly correspond to one of the subsurface echoes and cannot be unambiguously attributed to an off-nadir surface feature.

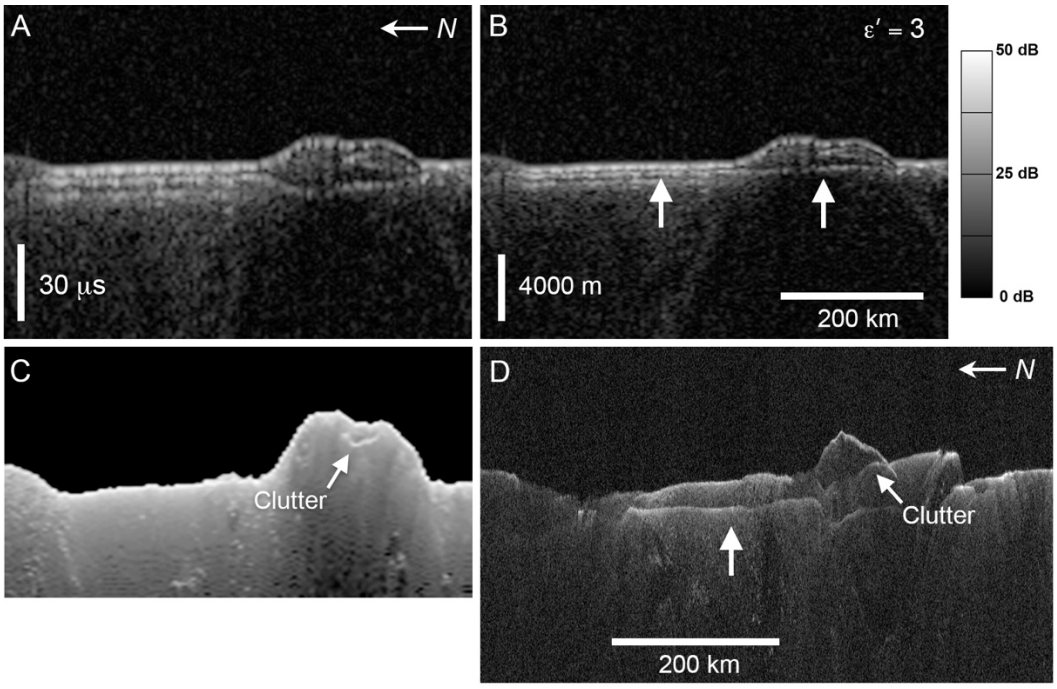

Figure S4. Radargrams of a portion of MARSIS SS3 orbit 13416, band 2. The orbit crosses deposits of Amazonis Mensa-Gordii Dorsum and the intervening saddle region near orbit 10216 (see Fig. 1, 2A). A)

Evidence of multiple subsurface echoes in the thick deposits of Amazonis Mensa. Relatively bright echoes in the saddle region of the deposit indicate two interior layers, while echoes in Amazonis Mensa proper suggest at least three interior layers. B) Radargram showing orbit 13416, band 2 converted to depth using a dielectric constant $\varepsilon' = 3$. The depth-corrected radargram shows that the basal echo in Amazonis Mensa corresponds to the shallow subsurface echo in the saddle region (between Amazonis Mensa and Gordii Dorsum) as highlighted by the two arrows. C) A clutter simulation (McMichael et al., 2017) generated using MOLA (the approximate area of the model corresponding to the radargram shown in A). D) Portion of SHARAD orbit 24211_01 over the same region of Amazonis Mensa/saddle/Gordii Dorsum, which further confirms that a single, continuous reflector extends below the saddle and Amazonis Mensa, which we interpret to be the base of the deposits (large arrow). The deeper echoes in the saddle region is likely a stratigraphically lower contact in the sequence of lowland basalts, or an earlier deposit of MFF material. The shallow reflector at Δt ~4.3 μs in the Amazonis Mensa-Gordii Dorsum valley (large arrow) is interpreted to be the transition between the MFF and basaltic plains flow units separated by earlier deposits of MFF material (see Morgan et al., 2015). The intermediate reflector (small arrow) is a clutter feature.

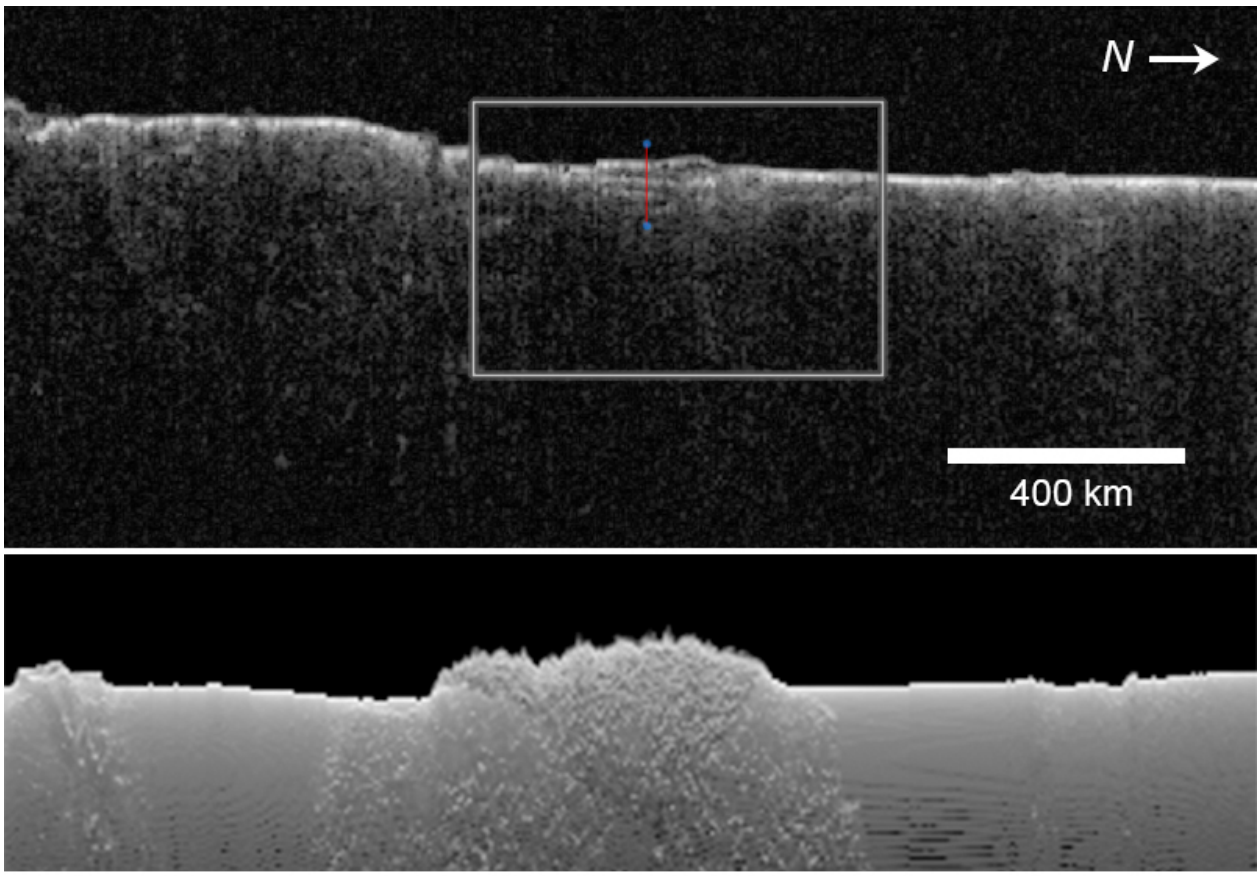
N
400 km

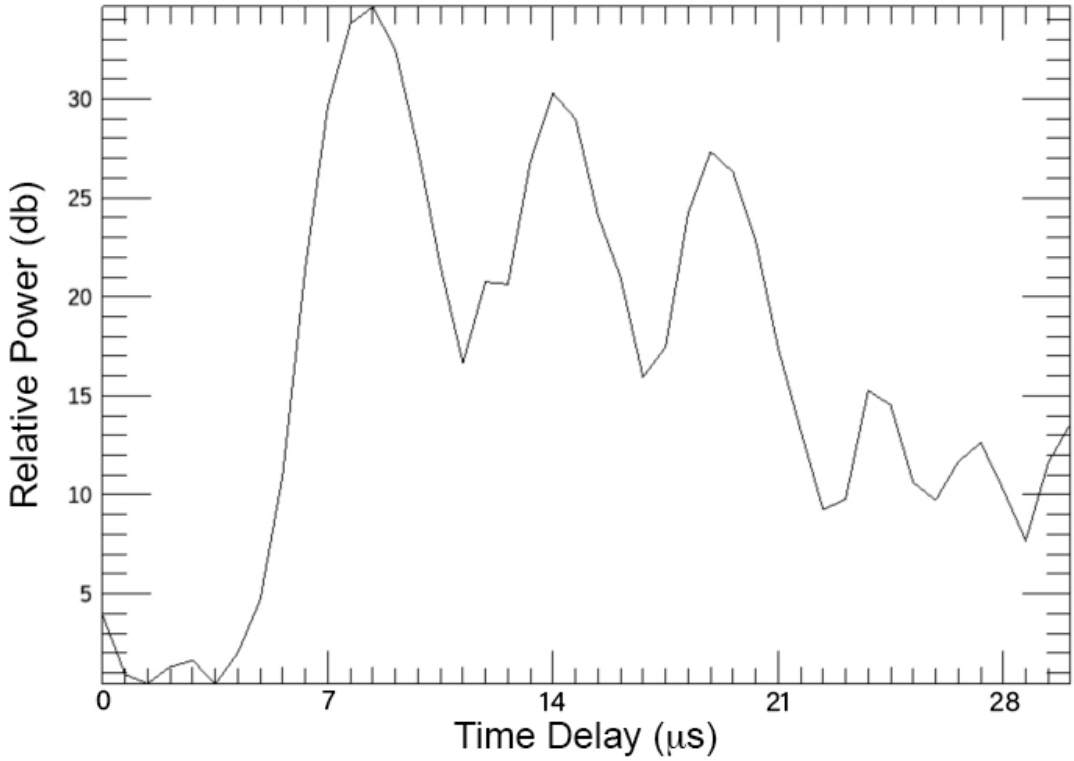
Relative Power (db)
30
25
20
15
10
5
0
7
14
21
28
Time Delay (μs)

Figure S5. Radargram and relative echo power versus time delay for MARSIS SS3 orbit 10121, band 3. The orbit crosses deposits of Amazonis Mensa-Gordii Dorsum (see Fig. 1, 2A). The four peaks in relative power are interpreted to be the surface return (largest peak) and three subsurface echoes, with the echo at greatest time delay from the surface return is interpreted to be the basal interface. A clutter simulation (McMichael et al., 2017) generated using MOLA topography is shown in the middle panel (the approximate area of the model corresponding to the radargram is show by the rectangular box). The clutter model shows no echoes from off-nadir surface features that account for the observed subsurface echoes in the radargram.

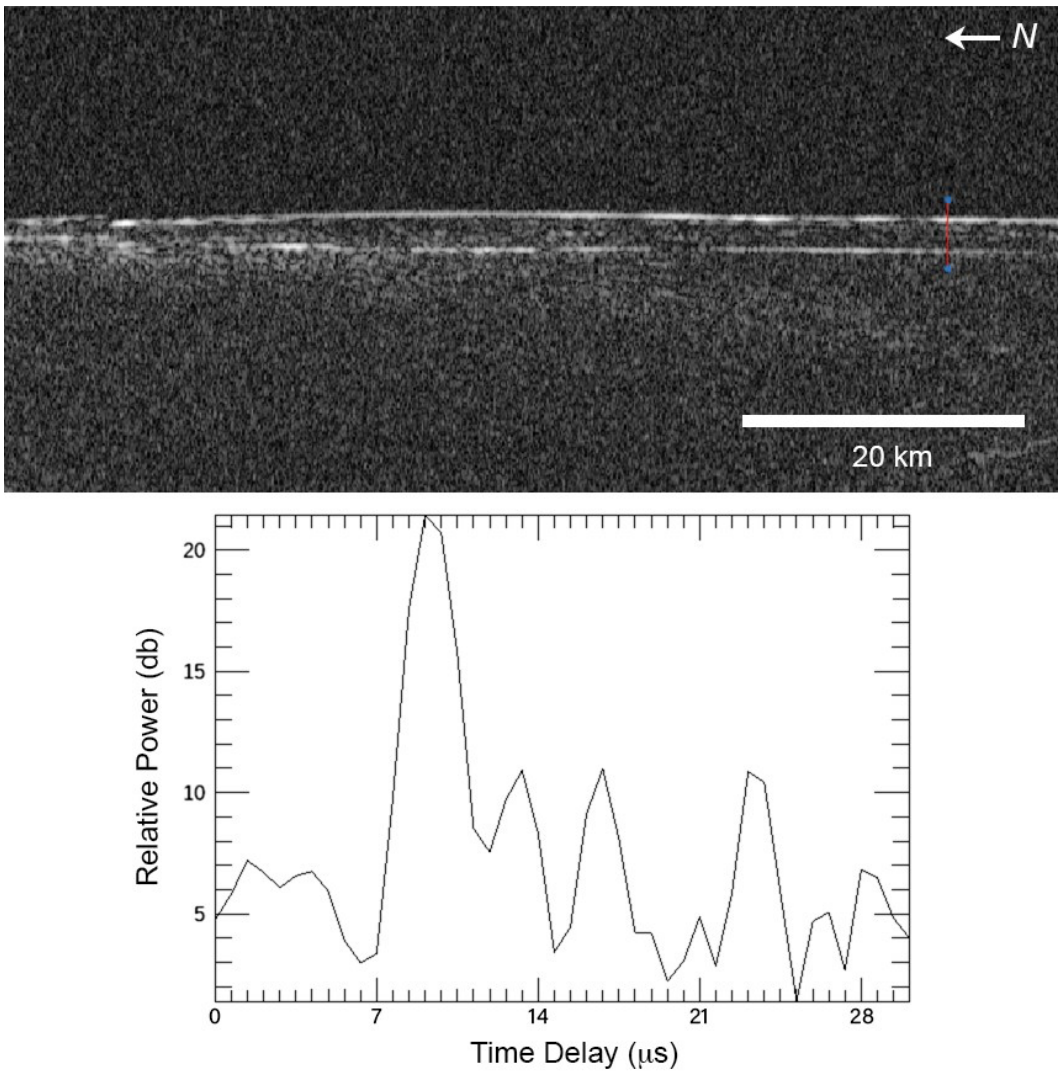

Figure S6. Radargram and relative echo power versus time delay for MARSIS SFM orbit 19681, band 2. The orbit crosses deposits of Amazonis Mensa-Gordii Dorsum (see Fig. 1, 2E). The four peaks in relative power are interpreted to be the surface return (largest peak) and three subsurface echoes, the two echoes closest in time delay to the peak echo are interpreted to be layers in the MFF deposits and the strong echo at greatest time delay is the basal interface. The two subsurface echoes are at Δt ~4.3 μs and Δt ~8.51 μs and the basal echo is at Δt ~14.18 μs. These layers are estimated to be at depths of ~370 m and 740 m, with a basal interface at a depth of ~1,230 m assuming $\varepsilon' = 3$.

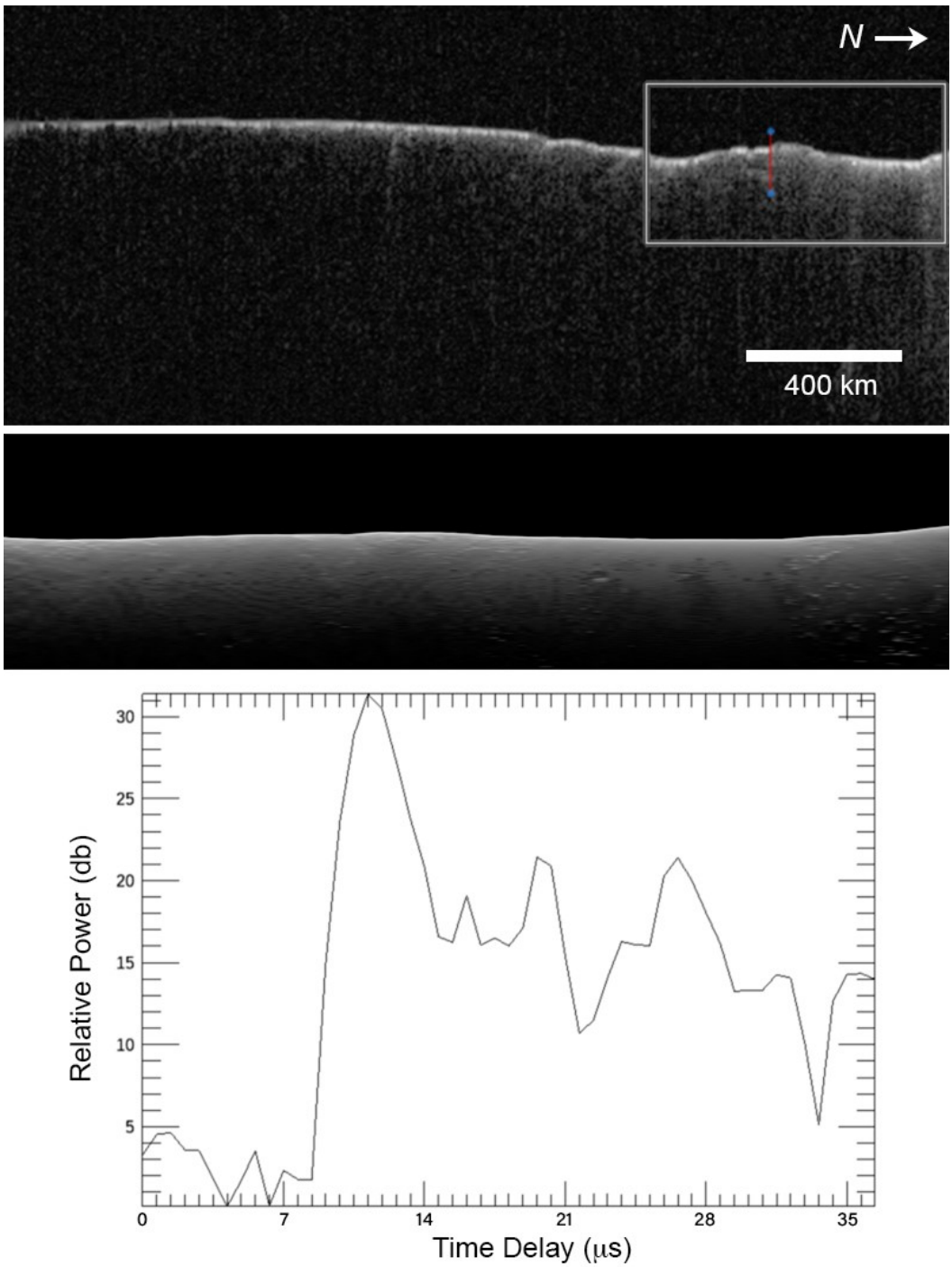

Figure S7. Radargram and relative echo power versus time delay for MARSIS SS3 orbit 08097, band 2. The orbit crosses deposits of Amazonis Mensa-Gordii Dorsum near Gigas Fossae (see Fig. 1). The three peaks in relative power are interpreted to be the surface return (largest peak) and two subsurface echoes, the echo close in time delay to the peak echo is interpreted to be a shallow layer in the deposits

and the strong echo at greatest time delay is the basal interface. With a Δt of ~8.51 μs and ~15.6 μs and assuming a real dielectric constant ε′ of ~3, the corresponding depths are ~740 m and ~1,350 m. A clutter simulation (McMichael et al., 2017) generated using MOLA topography is shown in the middle panel (the approximate area of the model corresponding to the radargram is show by the rectangular box). The clutter model shows no echoes from off-nadir surface features that account for the observed subsurface echoes in the radargram.

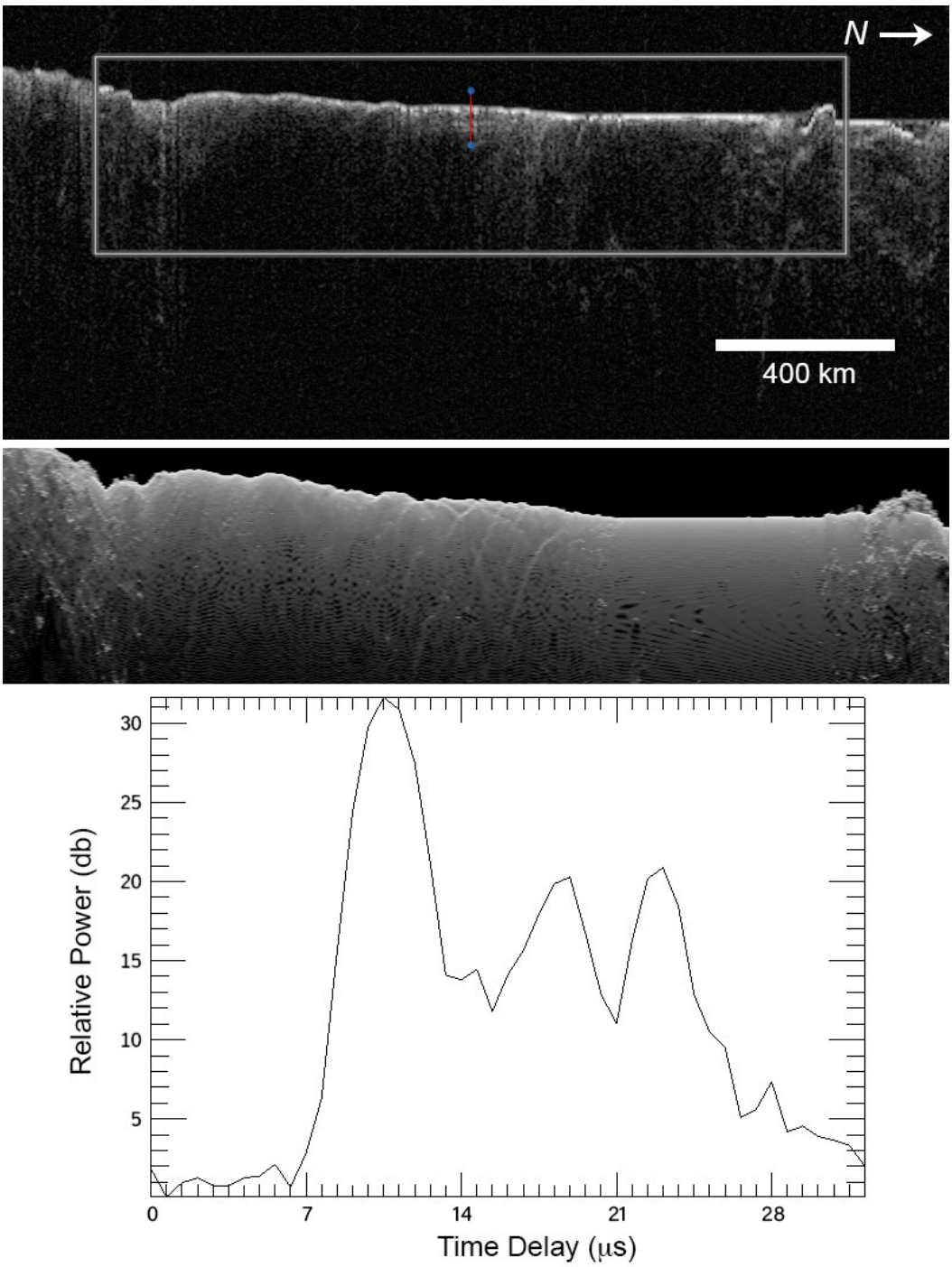

Figure S8. Radargram and relative echo power versus time delay for MARSIS SS3 orbit 18703, band 4. The orbit crosses Medusae Fossae Formation deposits of Lucus Planum (see Fig. 1, 2F). The three peaks in relative power are interpreted to be the surface return (largest peak) and two subsurface echoes from the basal interface, at greatest time delay, and an intermediate depth layer. With a Δt of ~8.51 μs and

~12.76 μs and assuming a real dielectric constant ε′ of ~3, the corresponding depths are ~740 m and ~1,110 m. A clutter simulation (McMichael et al., 2017) generated using MOLA topography is shown in the middle panel (the approximate area of the model corresponding to the radargram is show by the rectangular box). The clutter model shows no echoes from off-nadir surface features that account for the observed subsurface echoes in the radargram.

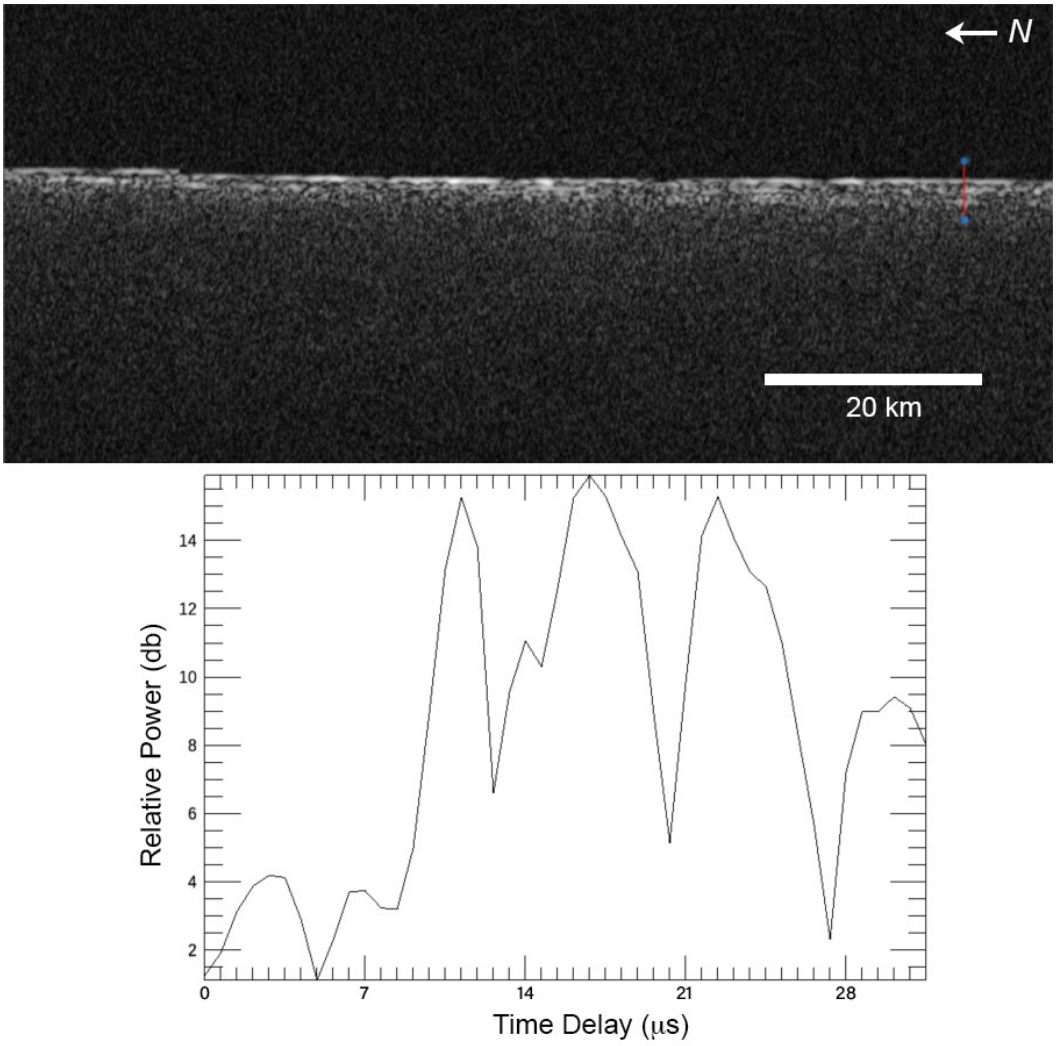

Figure S9. Radargram and relative echo power versus time delay for MARSIS SFM orbit 19738, band 2. The orbit crosses deposits of Zephyria Planum (see Fig. 1, 2F). The four peaks in relative power are interpreted to be the surface return (largest peak) and three subsurface echoes, the two echoes closest in time delay to the peak echo are interpreted to be layers in the MFF deposits and the strong echo at

greatest time delay is the basal interface. The subsurface echoes at Δt ~5.67 μs has a corresponding depth of ~490 m with a basal interface at Δt ~11.35 μs and a depth of ~980 m assuming $\varepsilon' = 3$.

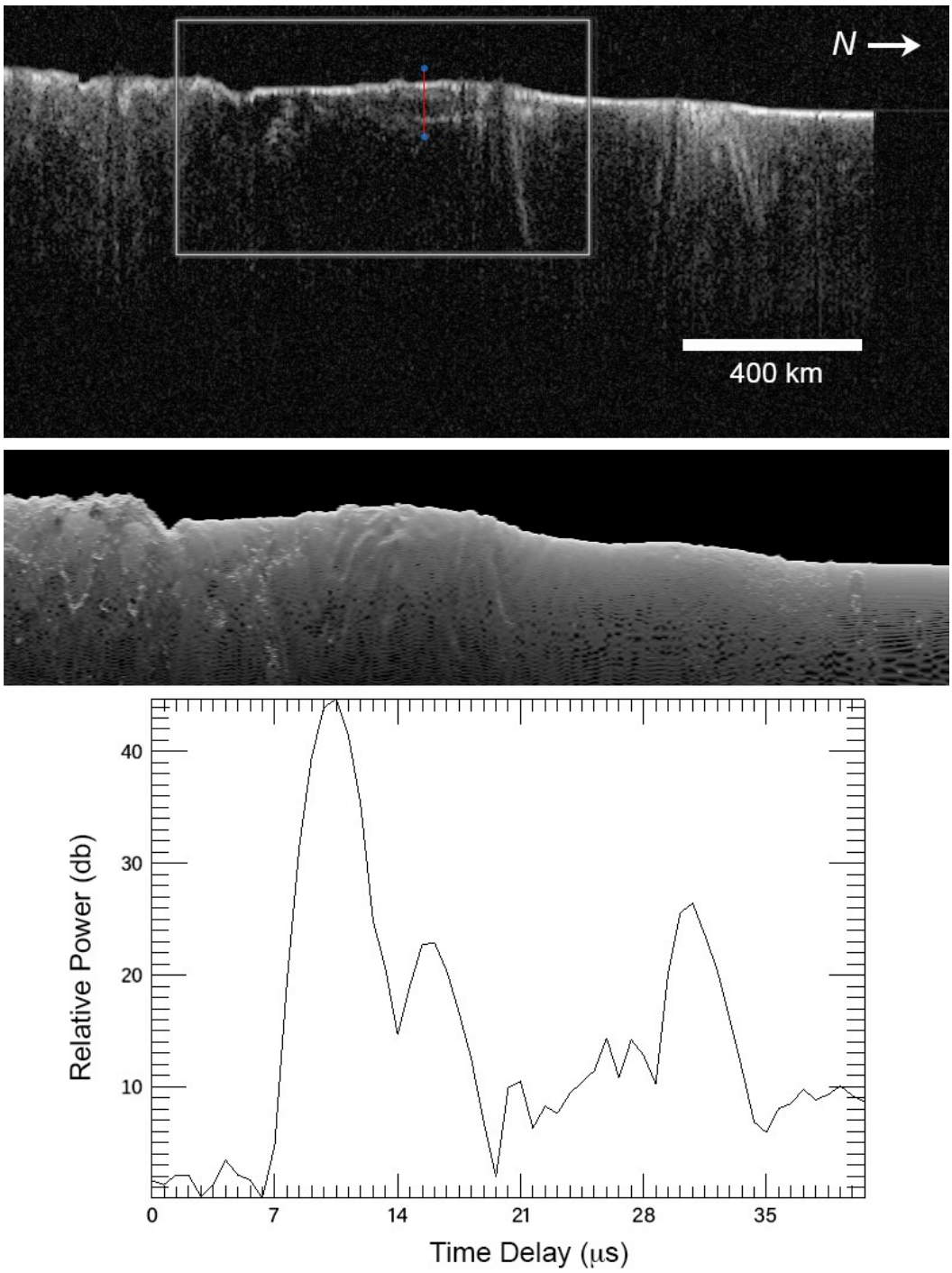

Figure S10. Radargram and relative echo power versus time delay for MARSIS SS3 orbit 18664, band 2. The orbit crosses deposits of Medusae Fossae-Eumenides Dorsum (see Figs. 1, 2G). The three peaks in relative power are interpreted to be the surface return (largest peak) and two subsurface echoes, the echo close in time delay to the peak echo is interpreted to be a shallow layer in the deposits and the

strong echo at greatest time delay is the basal interface. With a Δt of ~5.67 μs and ~20.57 μs and assuming a real dielectric constant ε′ of ~3, the corresponding depths are ~490 m and ~1,780 m. A clutter simulation (McMichael et al., 2017) generated using MOLA topography is shown in the middle panel (the approximate area of the model corresponding to the radargram is show by the rectangular box). The clutter model shows no echoes from off-nadir surface features that account for the observed subsurface echoes in the radargram.

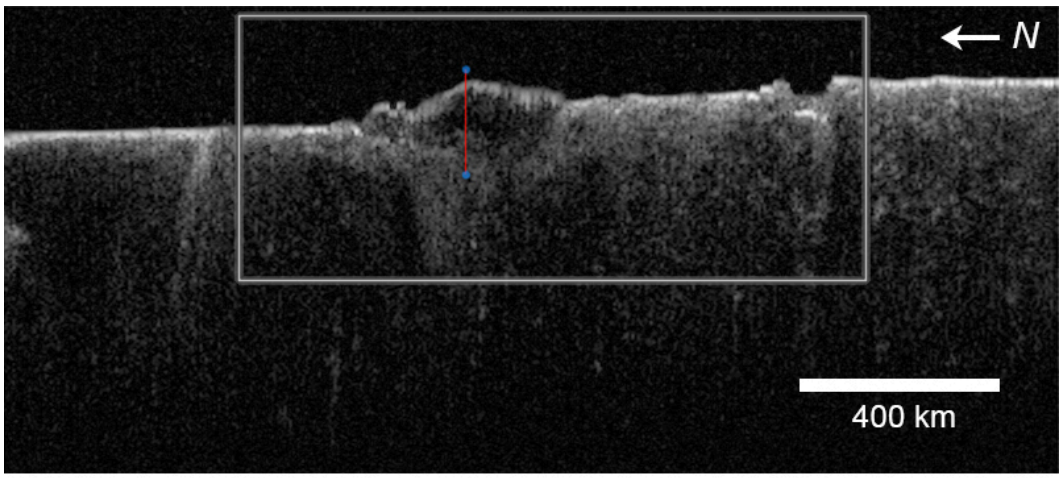
N
400 km

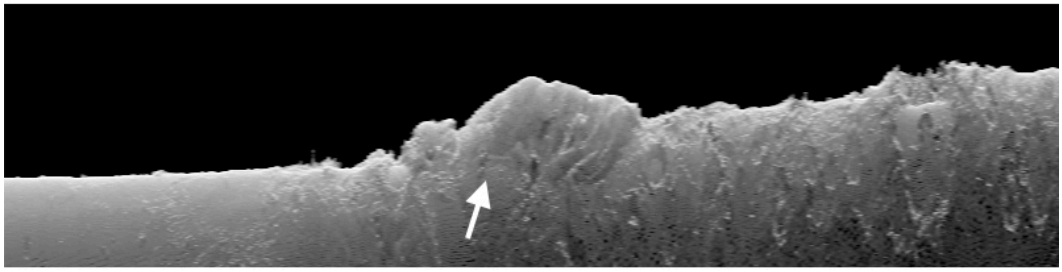

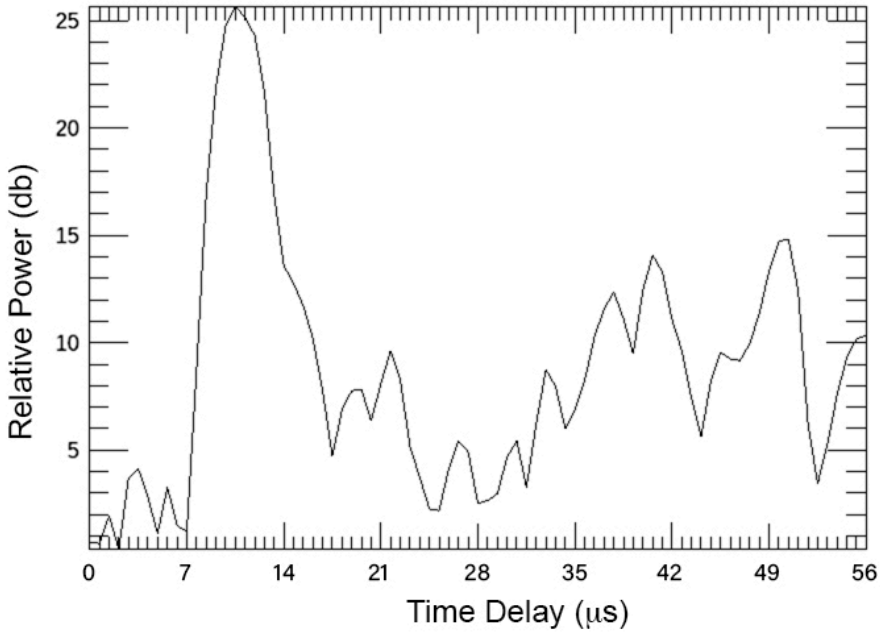
Relative Power (db)
25
20
15
10
5
0
7
14
21
28
35
42
49
56
Time Delay (μs)

Figure S11. Radargram and relative echo power versus time delay for MARSIS SS3 orbit 13240, band 2. The orbit crosses deposits of Eumenides Dorsum where its relief reaches a maximum (see Fig. 1, 3A). The peak in relative power is interpreted to be the surface return (largest peak) and the strong echo furthest in time delay is the basal interface of the MFF deposits overlying Amazonian volcanic plains. A clutter simulation (McMichael et al., 2017) generated using MOLA topography is shown in the middle panel (the approximate area of the model corresponding to the radargram is show by the rectangular box). The clutter model shows two linear features close in time delay (arrow) to the diffuse basal echoes in 13240, however, they do not match in delay, geometry or extent of the basal echoes. Thus, although the clutter features may contribute, no echoes from off-nadir surface features unambiguously account for the observed subsurface echoes in the radargram.

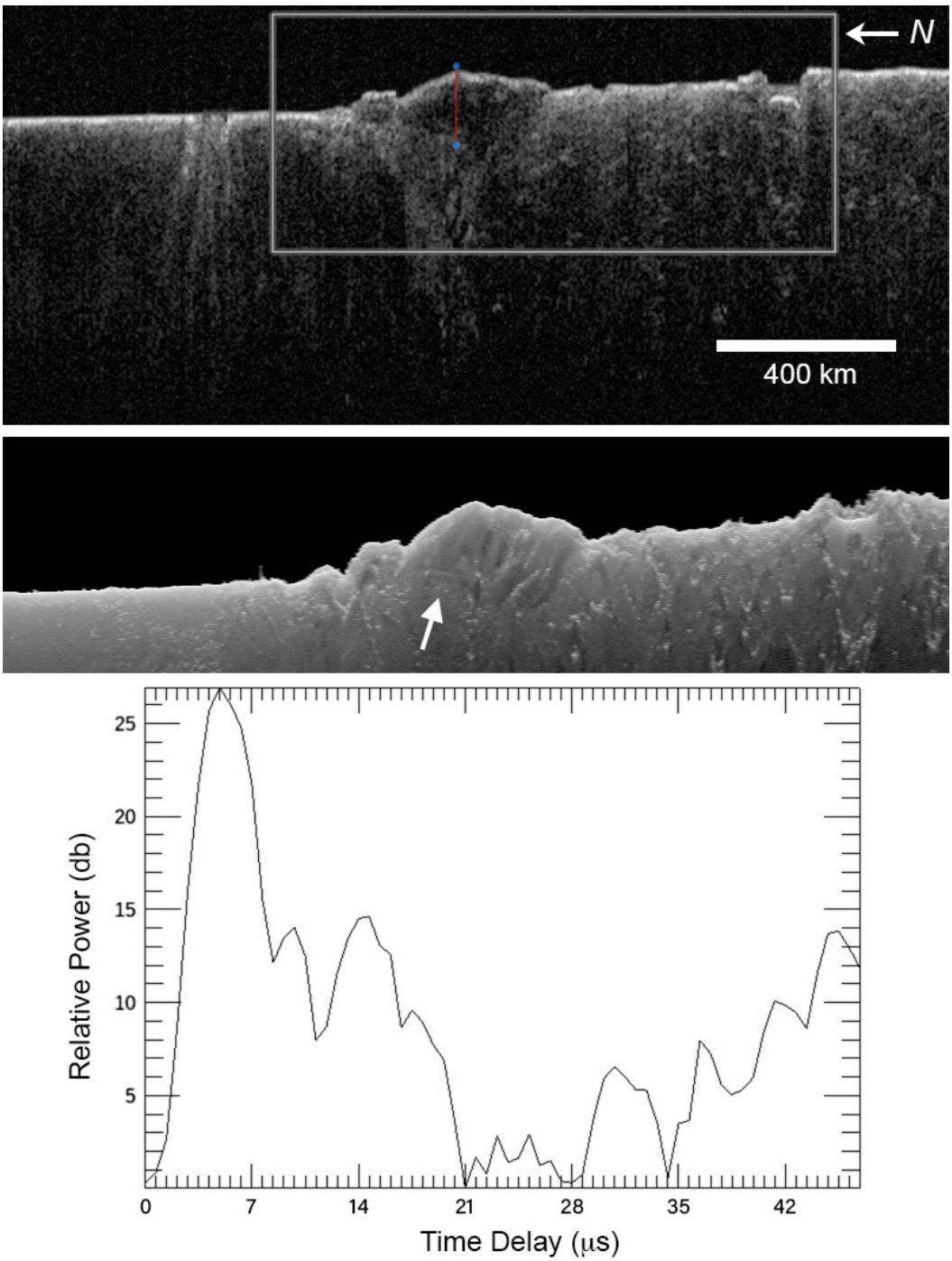

Figure S12. Radargram and relative echo power versus time delay for MARSIS SS3 orbit 15423, band 2. The orbit crosses deposits of Eumenides Dorsum where its relief reaches a maximum (see

Fig. 1, 3B). The peak in relative power is interpreted to be the surface return (largest peak) and the strong echo furthest in time delay is the basal interface of the MFF deposits overlying Amazonian volcanic plains. A clutter simulation (McMichael et al., 2017) generated using MOLA topography is shown in the middle panel (the approximate area of the model corresponding to the radargram is show by the rectangular box). The clutter model shows a linear feature close in time delay (arrow) to the diffuse basal echoes in 15423, however, it does not match in delay, geometry, or extent of the basal echoes. Thus, although the clutter features may contribute, no echoes from off-nadir surface features unambiguously account for the observed subsurface echoes in the radargram.

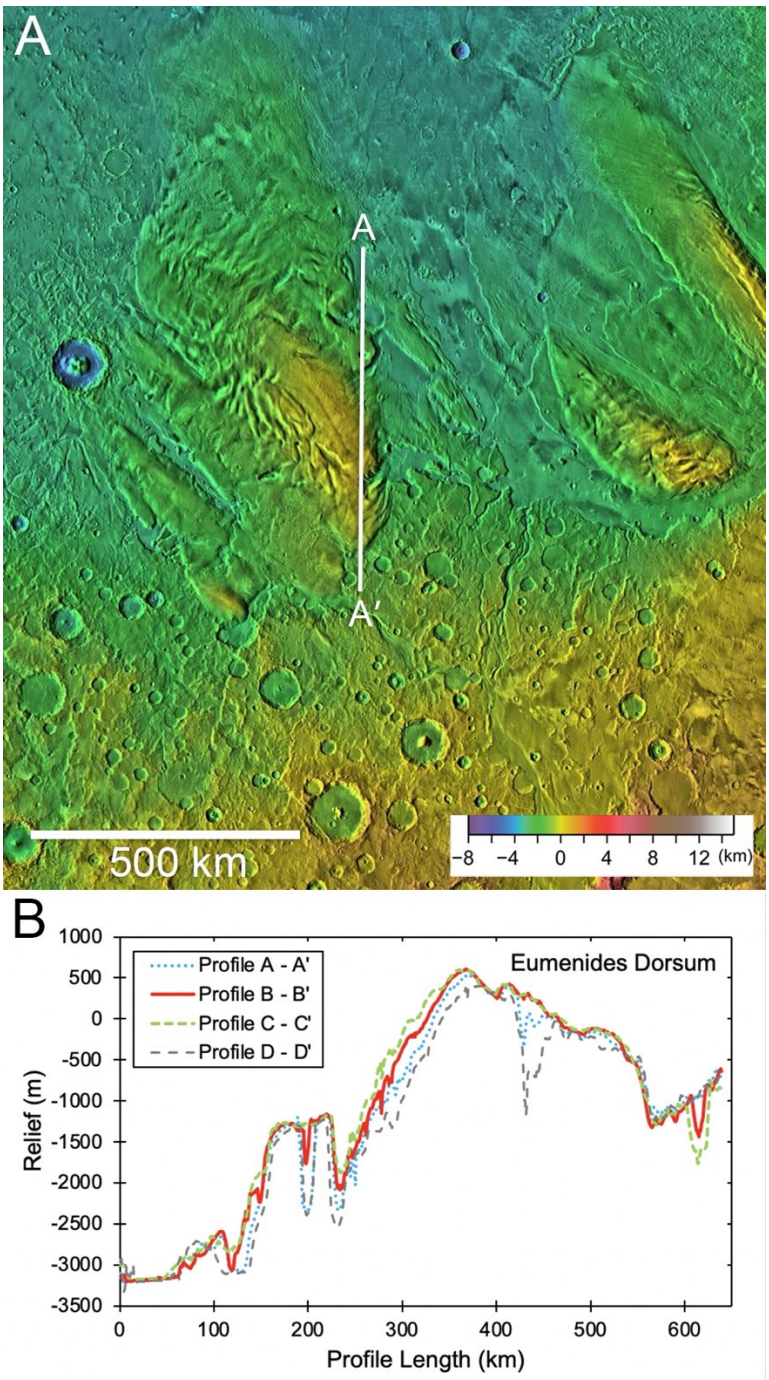

Figure S13. Topography of Eumenides Dorsum. A) MOLA shaded relief map with colorized elevation of the Eumenides Dorsum region. B) Topographic profiles across area where ground track of orbits 13240 and 15423 are located. The local mean maximum relief is ~3,700±90 m. The location of the profiles is shown in S13A, all four profiles adjoin profile A-A′. See elevation scalebar in Figure 1.

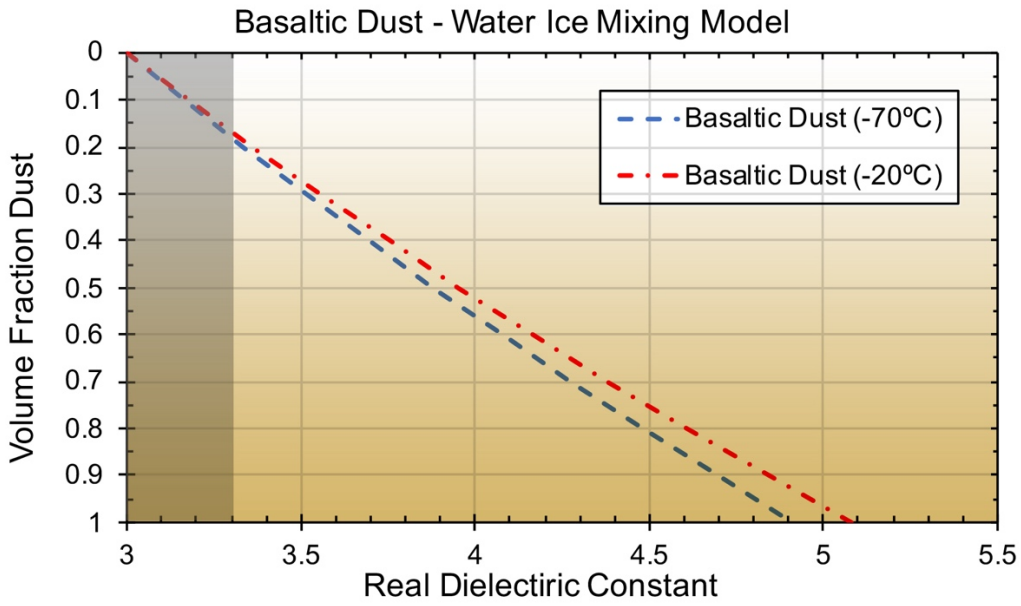

Figure S14. Plot of the real dielectric constant as a function volume fraction of basaltic dust and water ice in a mixture. The real dielectric constants of basaltic dust in the model are 4.91 at –20°C and 5.08 at –70°C (Heggy *et al*., 2008). The volume fraction of air is assumed to be 0. The area in gray shows the range in estimates of ε′ for the MFF deposits ≥ 3 (Watters et al., 2007).

References

Andrews-Hanna, J.C. et al., Meridiani Planum and the global hydrology of Mars, *Nature* **446**, 163–166 (2007).

Athy, L.F., (1930) Density, porosity and compaction of sedimentary rocks, *Amer. Assoc. Petro. Geophys. Bull.* **14**, 1-24.

Binder A.B. & Lange, M.A. (1980) On the Thermal History, Thermal State, and Related Tectonism of a Moon of Fission Origin, *Moon* **17**, 29-45.

Brouet Y. *et al*., (2019) A laboratory-based dielectric model for the radar sounding of the martian subsurface, Icarus **321**, 960-973.

Campbell, B.A., Watters, T.R., Morgan, G.A. Dielectric Properties of the Medusae Fossae Formation and Implications for Ice Content, *J. Geophys. Res*., doi:10.1029/2020JE006601 (2021).

Carter L.M. *et al*., (2009) Shallow Radar (SHARAD) sounding observations of the Medusae Fossae Formation, Mars, *Icarus* **199**, 295-302.

Clifford, S.M. (1993) A Model for the Hydrologic and Climatic Behavior of Water on Mars, *J. Geophys. Res.* **98**, 10,973-11,016.

Domenico P.A. & Mifflin, M.D. Water form low-permeability sediments and land subsidence, *Water Resources Res.* **1**, 563-576 (1965).

Freeze R.A. & Cherry, J. *Groundwater,* Pearson Publishing (1979).

Grotzinger, J.P. et al., (2015) Deposition, exhumation, and paleoclimate of an ancient lake deposit, Gale crater, Mars, Science 350 DOI: 10.1126/science.aac7575.

Gromov, V.V., Physical and mechanical properties of Lunar and Planetary Soils, in *Laboratory Astrophysics and Space Research*, edited by Ehrenfreund P. et al.) pp. 121-142, Kluwer Academic Publishers (1999).

Hantschel T. & Kauerauf, A. I. (2009) *Fundamentals of Basin and Petroleum Systems Modeling,* Springer-Verlag, Berlin.

Heggy E. *et al*., (2008) On the Dielectric Properties of Dust and ice-dust mixtures: Experimental Characterzation of the Martian Polar Layered Deposits Analog Materials, *LPSC 38th*, Abstract #1756.

Hapke B. & Sato, J. The porosity of the upper lunar regolith, *Icarus* **273**, 75-83 (2016).

Head J.W. & Kreslavsky M., Medusae Fossae Formation: Ice-Rich Airborne Dust Deposited During Periods of High Obliquity, *Lunar Planet. Sci.* **35**, 1635 (abstr.) (2004).

Jordan, R. et al., (2009) The Mars express MARSIS sounder instrument, *Planet. Space. Sci.* **57**, 1975-1986.

Kawabata E. et al., Identifying multiple eruption phases from a compound tephra blanket: an example of the AD1256 Al-Madinah eruption, Saudi Arabia, *Bull. Volcanology* **77**, doi10.1007/s00445-014-0890-y (2015).

Lewis K.W. et al., (2019) A surface gravity traverse on Mars indicates low bedrock density at Gale crater, *Science* **363,** 535–537.

McMichael J.G., Gim, Y. Arumugam D.D. and Plaut, J.J. *2017 IEEE Radar Conference (RadarConf)*, 2017, pp. 0873-0878, doi: 10.1109/RADAR.2017.7944326.

Mitchell, J.K. et al., Mechanical properties of lunar soil: Density, porosity, cohesion, and angle of internal friction, *Proc. Lunar Sci. Conf.* 3, 3235-3253 (1972).

Morgan, G.A. *et al*., (2015) Evidence for the episodic erosion of the Medusae Fossae Formation within the youngest volcanic province on Mars, *Geophys. Res. Lett*. **42**, 7336–7342.

Paladio-Melosantos M.L.O. et al., in *Fire and Mud: Eruptions and Lahars of ount Pinatubo, Philippines*, edited by Newhall, C. G. and Punongbayan, R. S.) Univ. of Washington Press (1997).

Palmer S.J. & H.W. Wick, *New Zealand Geotechnical Society Symposium*, 240-250 (2003).

Pender, M. J. et al., (2006) Geotechnical properties of a pumice sand, Soils and Foundations, **46**, 69-81.

Schultz P.H. & Lutz, A.B. Polar wandering of Mars, *Icarus* **73**, 91 (1988).

Stillman D.E. et al., (2010) Low-Frequency Electrical Properties of Ice-Silicate Mixtures, *J. Phys. Chem.* **114**, 6065-6073.

Squyres, S.W. et al., In Situ Evidence for an Ancient Aqueous Environment at Meridiani Planum, Mars, *Science* 306, 1709–1714 (2004).

Tanaka K.L. *et al*., (2014) Geologic map of Mars: U.S. Geological Survey Geologic Investigations 3292, https://dx.doi.org/10.3133/sim3292.

Watters T.R. *et al*., MARSIS radar sounding of the Medusae Fossae Formation: A unique deposit on Mars, *Science* **318**, 1125–1128 (2007).

Watters T.R. *et al.*, Radar sounder evidence for a thick, porous sediments in Meridiani Planum and Implications for ice-filled deposits on Mars, *Geophys. Res. Lett.* **44**, 9208–9215 (2017).

Wilson T.M. et al., (2012) Volcanic ash impacts on critical infrastructure, *Phys. Chem. Earth,* **45-46**, 5-23.